30-year record of Himalaya mass-wasting reveals landscape perturbations by extreme events

***Joshua N. Jones (1, 2), Sarah J. Boulton (2), Georgina L. Bennett (3), Martin. Stokes (2), Michael R. Z. Whitworth (4)**

[1]*School of Environmental Sciences, University of East Anglia, Norwich Research Park, Norwich, NR4 7TU*

[2]*School of Geography, Earth and Environmental Sciences, University of Plymouth, Drakes Circus, Plymouth, PL4 8AA*

[3]*College of Life and Environmental Sciences, Geography, University of Exeter, Amory Building, Rennes Drive, EX4 4RJ*

[4]*AECOM, East Wing Plumer House, Tailyour Road, Plymouth, PL6 5DH*

*Joshua N. Jones; Joshua.N.Jones@uea.ac.uk / joshua.jones@plymouth.ac.uk, @joshjones06

Sarah. J. Boulton; sarah.boulton@plymouth.ac.uk, @geologySarah

Georgina L. Bennett; G.L.Bennett@exeter.ac.uk, @DrGeorgieB

Martin. Stokes; m.stokes@plymouth.ac.uk

Michael R. Z. Whitworth: michael.whitworth@aecom.com, @geo_whitworth

Abstract

In mountainous environments, quantifying the drivers of mass-wasting is fundamental for understanding landscape evolution and improving hazard management. Here, we quantify the magnitudes of mass-wasting caused by the Asia Summer Monsoon (ASM), extreme rainfall and earthquakes in the Nepal Himalayas. Using a newly compiled 30-year mass-wasting inventory, we establish empirical relationships between monsoon-triggered mass-wasting and ASM precipitation before quantifying how other mass-wasting drivers have perturbed this relationship. We find that perturbations up to 5 times greater than that expected from the ASM alone are caused by rainfall events with 5 to 30 year return periods and short-term (< 2 year) earthquake-induced landscape preconditioning. In 2015, the landscape preconditioning induced perturbation is found to be strongly controlled by the topographic signature of the Gorkha earthquake, whereby high Peak Ground Acceleration (PGA) coincident with excess topography (rock volume above a landscapes threshold angle) amplifies landscape damage.

Introduction

In mountainous terrain, mass-wasting processes dominate landscape evolution [1–3] posing serious risk to life and socioeconomic development [4,5]. Background rates of mass-wasting are driven by tectonic uplift [1,6] and climate [7–9], though their relative contributions over geological timescales are difficult to unravel [10]. At shorter timescales, mass-wasting background rates are perturbed by a variety of low-frequency, high-magnitude drivers including extreme rainfall, earthquakes and floods [11–14]. Quantifying and unravelling mass-wasting caused by such diverse sets of drivers is fundamental in efforts to forecast and mitigate mass-wasting hazards in response to environmental change.

Compilation and comparison of erosion rates measured over different timescales can isolate the roles of different mass-wasting drivers. Such approaches typically utilize proxies including cosmogenic nuclides or suspended sediment flux to establish long-term background erosion rates against which shorter term perturbations captured by field sampling or remote sensing can be measured [2,12,13,15]. However, these approaches are inherently uncertain, with different methods over different timescales producing significantly different results [16]. Instead, a growing archive of remote sensing data is enabling the compilation of sufficiently long data sets of mass-wasting over large regions from which background mass-wasting rates can be established, and perturbations above the background rate identified [7,17]. However, due to the time-consuming nature of developing such long-term datasets, rarely have studies been able to unravel the relative impacts of diverse and interacting drivers acting on a landscape.

A region with a particularly complex set of interacting mass-wasting drivers, and one of the highest rates of mass-wasting on Earth [4], is the Himalaya Arc. High rates of tectonic uplift and the Asia Summer Monsoon (ASM) drive high background rates of mass-wasting [15,18–20], which are perturbed by extreme events including floods [21], extreme rainfall [22,23] and earthquakes [3,24]. However, the relative impacts of these drivers on mass-wasting remains unquantified, as most studies focus on the impacts of individual drivers. Thus, the fundamental baseline mass-wasting rate related to the ASM remains uncertain [3]. Indeed, whilst relationships between precipitation intensity and short-term suspended fluvial sediment flux in the Himalaya are well described [15,19,25], an empirical relationship between ASM strength and ASM-triggered mass-wasting in the central-eastern Nepal remains elusive [3]. This is problematic, as demonstrated by the 2015 M_w 7.8 Gorkha earthquake. As well as triggering over 24,000 coseismic landslides [24,26], the Gorkha earthquake caused elevated rates of new monsoon-triggered mass-wasting in the 2015 monsoon season, as a result of surface damage by seismically-induced strong ground motion [3], an effect termed earthquake preconditioning [17,27]. However, the timescale and magnitude of this preconditioning perturbation remains uncertain, as without empirical relationships between ASM precipitation and mass-wasting, it is challenging to distinguish whether post-earthquake mass-wasting from 2016 onwards was actually perturbed above the rate expected given the ASM strength [3]. As such, until an empirical relationship between ASM strength and mass-wasting volume is defined, our ability to understand and quantify mass-wasting perturbations due to extreme events across central-eastern Nepal is limited, thus impeding efforts to account for extreme events in forecasts of mass-wasting and in time-dependent models of landslide susceptibility.

Here, we quantify the mass-wasting impacts of the ASM, extreme rainfall and earthquake preconditioning in the Nepal Himalaya. We use a new 30-year mass-wasting inventory for central-eastern Nepal to establish empirical relationship between metrics of ASM strength and mass-wasting. These relationships are then used to calculate ASM strength-normalised rates of mass-wasting between 1988 and 2018. These normalised rates, alongside further inventory analysis, allows us to isolate and quantify the magnitudes and timescales of mass-wasting perturbations above that attributable to the ASM. As well as providing insight into the processes controlling landscape evolution, this allows further investigation into the characteristics and processes of earthquake preconditioning of hillslopes in the Himalayas.

Results

Mass-wasting inventory

Using visual inspection of Landsat 4/5/8 imagery, we mapped a 30-year inventory of rainfall-triggered mass-wasting across a ~42,000 km^2 region of central-eastern Nepal between 1988 and 2018 (Fig. 1; see methods). We mapped 12,920 moderate to large (>1000 m^2) mass-wasting events, whereby 10,138 were identified as new failures and 2,782 as reactivations or remobilisations of previous failures. Mapping occurred across 29 individual time slices, where each time slice encompassed a given year's monsoon season (approx. May – September) as well as a varying number of months either side. Note that the inventory does not include new coseismic or anthropogenic mass-wasting, though will include rainfall-induced reactivations/remobilisation of coseismic mass-wasting (see methods).

Empirical relationship between the ASM and mass-wasting

To quantify an empirical relationship between the ASM and mass-wasting, we first derive two measures of total mass-wasting for each time slice: 1) the volume of all mapped features, including new landslides, reactivations and remobilisations ("New + RR"); and 2) the volume of new features only, with reactivations and remobilisations removed ("New Only"). These measures allow us to isolate new post-earthquake mass-wasting related to earthquake damaged bedrock (i.e. earthquake preconditioning) from reactivations and remobilisations of coseismic and pre-existing mass-wasting. Both are significant for hazard assessment, but in this study we are primarily interested in the controls on new, and thus particularly unpredictable, mass-wasting in the landscape. For each measure, mass-wasting volumes were calculated using the global area-volume scaling relationships of Larsen et al. [28], both for estimated scar areas and total areas (combined scar, depositional and runout zones) (see methods).

For the mapped region, we then correlate all measures of mass-wasting volume for pre-Gorkha earthquake years with proxies for ASM strength derived from two rainfall products: PERSIANN-CDR [29,30] and APHRODITE [31] (see methods). For both PERSIANN-CDR and

APHRODITE, we use several proxies for ASM strength that have previously been investigated in the literature [3,32]. These proxies are: total May to September (MJJAS) precipitation, total precipitation from 15th July – end-September, total MJJAS precipitation > 25 mm (sum of all precipitation days with total rainfall values > 25 mm), and total precipitation > 25 mm from 15th July – end-September (sum of all precipitation days within this time periods with total rainfall values > 25 mm). Note that we avoid typical measures of monsoon strength such as the SASMI [33] as these are derived over extensive regional scales and so do not capture local changes in monsoon conditions. As previously observed in western Nepal [32],we find that for the PERSIANN-CDR data, total MJJAS precipitation provides the best fit to the mass-wasting data (Fig. 2a – d), whilst for APHRODITE, it is total MJJAS precipitation > 25 mm (Fig. 2e – h; see Supplementary Figs. S1 – 3 for all other sub-optimal correlations). Thus, from this point forward, the term "ASM strength" refers specifically to total MJJAS precipitation (mm/grid) for PERSIANN, and total MJJAS > 25 mm (mm/grid) for APHRODITE. Of the 24 pre-Gorkha earthquake years included in these correlations, we find that mass-wasting volume per unit area increases with total grid-averaged precipitation, with potential anomalies in 1989, 1993, 1995 and 2002 (R^2 = 0.69– 0.83 for non-anomalous years using PERSIANN-CDR (Fig. 2a – d) and R^2 = 0.56 – 0.67 for non-anomalous years using APHRODITE (Fig. 2e – h)).

The best-fit empirical relationships between ASM strength and mass-wasting (Fig. 2) were then used to derive ASM strength-normalised rates of mass-wasting across the entire mapped period (1988 – 2018). We undertake this normalisation using the methods of Marc et al., [17] (see methods), whereby the empirical relationships in Fig. 2a – h are used to calculate the predicted volumes of mass-wasting expected in each time slice based on that year's total grid averaged ASM strength. Then, for all measures of volume, by taking the ratio of the actual mapped volumes to the predicted volumes, we derived ASM strength-normalised rates of mass-wasting for each of the 29 time slices. These rates show that, for both rainfall products, most time-slices fall within a narrow band of mass-wasting around the expected normalised value of one, with several years clearly perturbed above this. For the PERSIANN-CDR normalisation, there are perturbations above +1 SD of the normal in 1993, 2002, and post-2015 (Fig. 3a). For the post-2015 perturbation, if coseismic reactivations and remobilisations are considered, then the years 2015 – 2016 are perturbed above the expected monsoons scaling, however, when considering only new failures, only 2015 is perturbed, as reported by Marc et al. [3]. For the APHRODITE normalisation, the years 1989, 1993, 2002 and 2015 are perturbed above + 1 SD of the normal, with another possible perturbation in 1995 (Fig. 3b).

As the ASM strength-normalised mass-wasting rate accounts for variance in ASM-precipitation, the identified perturbations should be attributable to infrequent high-magnitude mass-wasting drivers not accounted for by the metrics of ASM strength. However, before this can be assumed, it is important to show that these perturbations are not due to stochastic variation in mass-wasting areas, i.e., to confirm that the perturbations are not simply caused by a small number of anomalously large landslide events. We achieve this using two approaches (see also Methods). One, before correlating mass-wasting with ASM strength, we removed the largest landslides of each year if its scar area was greater than twice that of the second largest. This ensures that any large landslides that were affected by progressive failure across several monsoon seasons (e.g. the Jure landslide [34]), but failed catastrophically in one monsoon-season, are not incorrectly attributed to a single monsoon period [3]. Two, we fitted three-parameter inverse-gamma distributions to the Probability Density Functions (PDFs) of landslide area for all years combined, all pre-2015 non perturbed years, 1989, 1993, 1995, 2002, 2015 and all post-2015 years (Fig. 4a – h). If the inverse-gamma distributions fitted to each subset have similar scaling exponents (where a larger exponent indicates that larger landslides are contributing less to the overall inventory) and rollovers (the size above which power law behaviour applies), then we can rule out that the observed perturbations are caused solely by statistical anomalies in mass-wasting size.

Scaling exponents are found to fall within a narrow range of 1.8 – 2.2 for all subsets except 1995 and 2015, which had slightly lower exponents of 1.6. Similarly, the rollovers of most subsets fall within the range of 2000 – 6000 m^2, with the exception of 1989 and 1993, which had higher rollovers of 6000 – 7000 m^2. Overall, as the scaling exponents of the fitted distributions are similar above comparable cut-offs, the area-frequency distributions can be described as scaled versions of one another, though with 2015 and 1995 having a slightly higher proportion of large area events. This suggests that the observed perturbations are not solely attributable to stochastic change in mass-wasting size, but are due to physical processes increasing the frequency of all sizes of mass-wasting.

Impacts of extreme rainfall

The ASM strength-normalised rates identify mass-wasting perturbations in 1993, 1995 and 2002 that are not coincident with seismic activity > M_w 6.0 (Fig. 3a - b). If these perturbations are therefore associated with rainfall, we propose two explanations for their occurrence. One, they are due to years of overall intense monsoon activity that are poorly predicted by the normalisation method. Or two, they are due to significant rainfall events that occurred within the monsoon seasons but were too highly localised to be captured by the total monthly precipitation estimates. The time-series of monthly precipitation totals (Fig. 3a - b) show that the total monsoon rainfall for these years were not anomalously high. However, the perturbations in 1993 and 2002 were both coincident with "cloud-outburst" extreme rainfall events (e.g. Fig. 6). On 19-20th July 1993, > 540 mm of rainfall in 24 hours reportedly fell across a 500 km^2 region of the Kulekhani watershed, 30 km southwest of Kathmandu, causing over 1500 fatalities [22]. Similarly, on 23rd July, 2002, > 300 mm of rainfall in 24 hours reportedly fell across a 14,000 km^2 region of south-central Nepal, causing over 427 fatalities [35].

These reports suggest that the 1993 and 2002 mass-wasting perturbations were due to short-lived, localised, extreme rainfall events that were not recorded in the measures of ASM-strength. This raises several questions. How extreme were the events in 1993 and 2002? Did similarly extreme rainfall events cause or contribute to the other perturbations? Have other similarly extreme rainfall events occurred without triggering significant mass-wasting? What are the return periods of such events?

To answer these questions, it is necessary to define how extreme the 1993 and 2002 cloud outburst storm events were. To do this, we exploit the long (64 year) APHRODITE record of daily precipitation (1951 – 2015) to calculate Z-score anomalies for every monsoon-season (MJJAS) day across each of the 84 APHRODITE grids that encompass our study region. Thus, for each separate rainfall grid-cell, the mean and standard deviations of all monsoon-season days from 1951 to 2015 were calculated, and from this, individual daily Z-scores were obtained. A Z-score anomaly defines how many standard deviations a given observation is removed from the mean of a population. Z-score anomalies were used as they are a commonly used effective, method for semi-quantitatively assessing the change in environmental data [36,37].

For the 1993 and 2002 events, peak Z-scores were found to be ~12 and 16 – 19 respectively. To identify whether any similarly extreme rainfall events had occurred across our mapped time-period, we then extracted all days with Z-scores exceeding thresholds of 12, 14, and 16. We then correlated these with the normalisation results from Figure 3b (Fig 5a). This shows that just two other years observed rainfall events with Z-scores > 12, 1995, which also experienced a minor mass-wasting perturbation, and 2004, which did not. This tentatively suggests that a rainfall Z-score threshold of 12, relative to a grid-cells 1951 – 2015 long-term mean, is required to induce a significant mass-wasting perturbation above that expected from a typical ASM season. The perturbations in 2015 and 1989 do not coincide with any anomalously high rainfall, with neither year observing days with Z-scores > 10, suggesting that another process caused these perturbations.

As highlighted above, the 2004 monsoon season did not observe a mass-wasting perturbation, despite experiencing 8 cells (across the entire region) with Z-scores > 12 and 3 cells with Z-scores > 14. With the exception of 2002, which experienced Z-scores > 16, this year observed the most extreme rainfall between 1988 and 2015. There are two possible explanations for why the 2004 rainfall did not induce a mass-wasting response. One is that the extreme rainfall in 2004 occurred very early in the monsoon season (~June 15th), before hillslopes became fully saturated [3,38]. However, all 8 of cells expericing extreme rainfall in 2004 occurred after June 15th, so this seems unlikely. Two, is that the grid-cells experiencing extreme rainfall were located such that another process might explain why they did not experience significant mass-wasting. Figure 6 shows the locations of the 2004 extreme grids with Z-scores > 12, the permafrost extent of the region as defined by Gruber (2012) [39], and the grids that experienced perturbations in 2002. This highlights that the 2004 event was partially coincident with the extent of the 2002 event, with the cells that observed significant mass-wasting in 2002 (grid-cells 21, 22, 23) experiencing less mass-wasting in 2004 than those that did not (12, 11, 24). This could be because the 2002 event had already eroded much of the potential mass-wasting material from the landscape, and that significant volumes of new material had not re-accumulated by 2004. This tentatively suggests that following a large mass-wasting perturbation, the landscape requires several years to recover before it can experience a similar response, an observation that is comparable to the 10^0 - 10^2 post-extreme event recovery times estimated in other mountain ranges [40].

Overall, this analysis shows that the perturbations in 1993, 1995 and 2002 all correlate with years that experienced Z-scores > 12, suggesting that this is a threshold for which extreme rainfall can induce significant mass-wasting provided that the landscape has not recently observed another large erosion event. Thus, from hazard management and long-term erosional potential perspectives, it would be useful to know the return periods of such events. Based on the full 64 year time series of rainfall data, we calculate that across the entire study region, the return period of the 1993 event (Z-scores > 12) is ~4 years (15 events recorded in 64 years), and the return period of the 2002 event (Z-scores > 16) is ~33 years (2 events recorded in 64 years).

Impacts of earthquakes

There are two main processes by which large magnitude (> M_w 6.0) earthquakes can impact mass-wasting. First, large magnitude earthquakes can trigger coseismic landslides that can be remobilised by subsequent rainfall or other exhumation events [41–43]. Second, earthquake strong ground motion can induce landscape damage that induces enhanced rates of new post-earthquake mass-wasting [3]; a process termed earthquake preconditioning [27]. Earthquake preconditioning has been observed following multiple earthquakes in different geomorphic settings. For example, the 1999 M_w 7.7 ChiChi earthquake, Taiwan, caused a 2 – 5 year factor of 10 increase in subsequent new typhoon triggered landsliding [17], whilst the 1929 M_w 7.7 Buller earthquake, New Zealand, led to enhanced coseismic landsliding during the subsequent, partially coincident, 1968 M_w 7.1 Inangahua earthquake [27]. Similarly, the 25th April 2015 M_w 7.8 Gorkha earthquake, which occurred just prior to the onset of the 2015 monsoon season, is estimated to have caused a factor of 4 – 8 increase in new monsoon-triggered mass-wasting during the 2015 monsoon season [3]. However, the full timescale of 2015 preconditioning remains unconstrained as, until now, it has not been possible to isolate the earthquake preconditioning impacts from the monsoon in 2016 – 2018.

Here, our normalisation using the PERSIANN-CDR data (Fig. 3a) allows for the impacts of the 2015 earthquake and post-2015 monsoon to be separated, providing further insight into the magnitude and timescales of the 2015 preconditioning. In 2015, our normalisation with both PERSIANN and APHRODITE corroborates previous results [3], showing that all measures of mass-wasting were perturbed above that expected given the monsoon strength, with "New + RR" mass-wasting (which comprises new landslides, reactivations and remobilisations, including rainfall induced remobilisations of coseismic landslides) perturbed by a factor of 3.8 – 6.2 and "New Only" mass-wasting (where reactivations and remobilisations are excluded) perturbed by a factor of 2.4 – 4.6 (Fig. 3a - b). In 2016, we find that "New + RR" mass-wasting was still perturbed by a factor of 2.4 – 2.7, but that the "New Only" rate was within +1SD of the normal (Fig. 3a). In 2017 and 2018, both "New + RR" and "New Only" rates were back within +/- SD of the normal (Fig. 3a).

These results provide important insight into the timescales of the remobilisation of coseismic material, and of earthquake preconditioning associated with the Gorkha earthquake. For earthquake preconditioning, enhanced rates of new landsliding are only observed in 2015, with new landsliding in 2016 back to within +1 SD of that expected given the monsoon forcing. This suggests that Gorkha earthquake preconditioning lasted for 5 – 14 months, i.e., up until the start of the 2016 monsoon season. This timescale is slightly shorter than the 2 – 5 year preconditioning period observed in Taiwan following the ChiChi earthquake [17], but similar to the observations of Dahlquist and West [41] and Marc et al.,[3] who found that extra rainfall induced debris flows and landslides in Nepal following the Gorkha earthquake were anomalous in 2015 only. For the remobilisation of coseismic material, enhanced rates of mass-wasting when including remobilisations and reactivations, continues into 2016, but not 2017, suggesting a recovery time of 17 – 24 months. This recovery time is shorter than the 6 – 8 year period over which anomalous fluvial sediment export was observed following the ChiChi earthquake [43]. The timescale difference is likely because our approach only identifies large-scale remobilisations and reactivations, whereas measures of fluvial sediment export are more sensitive to small scale changes that would not be visible at the mapping resolution used here. The APHRODITE-based normalisation also identifies a perturbation in 1989. The 1989 monsoon season was the first full monsoon season following an M_w 6.9 earthquake that occurred on 21/08/1988. In this case, both the earthquake preconditioning perturbation ("New Only" rate) and increase in reactivations and remobilisations ("New + RR" rate) are observed in 1989 only, suggesting a recovery period for these processes of no more than 13 – 20 months, i.e. similar to that observed for the Gorkha and ChiChi earthquakes.

This analysis provides insight into short-term Himalaya preconditioning of the type observed by Marc et al., [17]. However, whilst our study and others have quantitatively constrained the magnitudes and timescales of short-term earthquake preconditioning, the processes and causal mechanisms remain uncertain. It has been proposed that short-term preconditioning occurs via near-surface earthquake damage that is rapidly exploited by subsequent rainfall as new failures [17], but what controls the spatial distributions of this damage is unclear.

To investigate what controls earthquake preconditioning damage, we combine our 2015 monsoon-triggered landslide inventory with Gorkha earthquake USGS ground motion data to examine how the excess-mass wasting observed in 2015 relates to the Gorkha earthquake PGA and other topographic factors. To do this we need to move from regional scale analysis to more localised, grid-scale analyses. As such, we divided our study region into the same 84 grid-cells as used for the Z-score analysis (Fig. 6). Then, using the approach detailed in the Methods, we calculated for each grid-cell the percentage change in 2015 monsoon-triggered mass-wasting relative to that grids non-perturbed mean, and the summed maximum PGA from both the M_w 7.8 Gorkha earthquake main shock and M_w 6.3 aftershock. We then plot the percentage change in 2015 monsoon-triggered mass-wasting against summed maximum PGA for all grids that experienced mass-wasting in 2015 and had less than 10% snow cover (Fig. 7a). Surprisingly, this shows no correlation between 2015 mass-wasting and PGA. This questions whether it is PGA alone that induces earthquake preconditioning. As seismic ground motion undergoes amplification when travelling across topographic excesses[44–46], earthquake preconditioning preferentially occurs where high PGA is coincident with high excess topography, where excess topography is defined as the volume of rock-mass above a landscape's threshold angle [47].

To investigate this, we calculate the average excess topography of each grid-cell for five landscape threshold angles (25°, 30°, 35°, 40°, 45°; see Methods). For each threshold of excess topography, we then calculate for every grid-cell the product of maximum summed Gorkha earthquake PGA's and average excess topography, and re-plot these weighted "PGA-Excess

Topography" values against each grid-cells 2015 percentage mass-wasting change. Fig. 7b shows the result for PGA-weighted by excess topography at a threshold angle of 45°. It is clear that there is a significant improvement of fit compared to using PGA alone, with R^2 increasing from 0.08 to 0.71. This result was consistent across all excess topography thresholds (Supplementary Figs. S4 - 5), but with a slight increase in R^2 as the threshold increased from 25 – 45°. This was also consistent when only summing PGAs > 0.1 and 0.2 g, though with lower R^2 values (Supplementary Figs. S6 - 7). These PGA values have been identified as possible thresholds which must be exceeded for landslides to be induced [48,49]; however, these new results suggest that lower PGA values can still contribute to preconditioning, even if they do not directly trigger coseismic landslides. Overall, this analysis suggests that short-term earthquake preconditioning damage is concentrated where PGA and high excess topography coincide. This is an important result that could allow for more accurate prediction of where and how much preconditioning should be expected in a landscape following a given magnitude earthquake. However, it should be noted that a similar relationship was not observed for the 1988 earthquake (Supplementary Fig. S8). Reasons for this anomaly could be: 1) The 1988 earthquake had much lower PGAs than 2015 (a maximum of 0.28g in 1988 compared to >0.74g in 2015); 2) The region impacted by the 1988 event was to the south of our study region, where excess topography values are low, or 3) The 1989 perturbation was actually caused by rainfall. Despite not having Z-scores as high as observed in 1993 or 2002, it did observe higher Z-scores than 2015 (scores of 10, compared to 8). As described previously, reason 3 had already been discounted due to the relatively low Z-scores in 1989. As such, it is likely that no single explanation can explain the 1989 perturbation, tentatively suggesting that it is due to a combination of both the earthquake and rainfall.

This analysis provides insight into short-term Himalaya preconditioning of the type observed by Marc et al., [17], but does consider any longer, decadal-scale preconditioning. Longer-term preconditioning is less frequently observed than the short-term, and could be caused by deeper bedrock damage that takes longer to be exploited . Such deep damage should still be exploitable by rainfall, if less rapidly than shallow damage, as rainfall is known to be capable of inducing deep seated landslides [3,50]. Furthermore, in New Zealand, coseismic landslides associated with the 1968 M_w 7.1 Inangahua earthquake occurred at greater rates where the landscape was likely damaged by the earlier 1929 M_w 7.7 Buller earthquake. This suggests that lasting landscape damage due to the earlier event was compounded by the second event. Here, we investigate whether the 2015 monsoon-triggered perturbation was similarly affected by any long-term damage from earlier earthquakes in 1934 (M_w 8.0), 1988 (M_w 6.9) and 2011 (M_w 6.9) (Fig. N), which may have been compounded by the 2015 Gorkha earthquake.

To test whether these earlier events contributed to the 2015 monsoon-triggered perturbation, we repeat our PGA-excess topography correlations but this time cumulatively summing the maximum PGA observed per grid cell from the 2011, 1988, and 1934 earthquakes. These results, with PGA alone and PGA multiplied by excess topography at a threshold of 45°, are shown in Fig. 7c - h (for correlations of PGA with other excess topography thresholds see Supplementary Figs. S4 - 5). If these events had a damage legacy that significantly compounded the Gorkha earthquake damage, we would expect the inclusion of their PGA to improve the observed fit between the percentage-change in 2015 ASM mass-wasting and PGA-excess topography. However, whilst the inclusion of 2011 PGA does slightly improve the fit (R^2 increase from 0.71 – 0.72), including the PGA from 1988 and 1934 worsens the fit. This suggests that whilst some element of 2011 damage may have remained in the landscape in 2015, there is no evidence to support that the events in 1934 and 1988 had any impact on the distribution of elevated monsoon-triggered mass-wasting in 2015. There are several potential explanations for this. One, the time since the events in 1988 and 1934 is too long, and any damage caused by them has already been exploited. The 1934 event was 81 years before Gorkha, over twice as long as the 39 years between the two earthquakes observed to induce preconditioning in New Zealand. Two, the magnitudes of the 1988 and 1934 events were too small to induce wide scale damage. This explanation is less likely, as the 1934 event was of comparable magnitude to 2015, which did cause landscape damage, whilst the 1988 event was of comparable magnitude to 2011, which possibly caused landscape damage. Three, the 1988 and 1934 events were too far from the region impacted by Gorkha for any significant damage to overlap. This is the most likely explanation, as despite being of magnitudes that should be capable of inducing landscape damage, both the 1934 and 1988 events occurred in southern Nepal, with no PGAs > 0.2g in 1988 and 1934 overlapping with PGAs > 0.1g in 2015 (Fig. 7a - b). The 2011 event also had no overlap with 2015 at PGAs > 0.1g, potentially explaining why this more recent event also had minimal, if any, impact on excess monsoon-triggered mas-wasting in 2015.

Overall, our earthquake analysis suggests that short term preconditioning is controlled by the topographic signature of earthquake damage, whereby preconditioning is induced only where high PGA is coincident with high excess topography, and that any damage induced by earlier earthquakes did not have a significant impact on the 2015 monsoon-triggered mass-wasting perturbation, likely because of a lack of overlap at high PGAs with the Gorkha earthquake.

Conclusions and implications

By quantifying a previously unknown empirical relationship between ASM strength and total mass-wasting we have been able to isolate and investigate mass-wasting perturbations due to extreme rainfall and 2015 Gorkha earthquake landscape preconditioning. We find that extreme, 4 – 33 year return period rainfall events can induce mass-wasting perturbations. However, we also find that the landscape takes time to recover from such events, with extreme rainfall in 2004 not inducing a perturbation due to its coincidence with the 2002 event. This tentatively suggests that large mass-wasting-inducing events can transiently reduce the likelihood of another extreme mass-wasting event occurring. The 2015 perturbation is found to be controlled by short-term landscape preconditioning induced by the 2015 Gorkha earthquake, the signature of which is controlled by the coincidence of PGA and excess topography. Finally, we find that earlier large magnitude earthquakes in 1934, 1988 and 2011 do not appear to have significantly compounded the 2015 preconditioning, suggesting that longer term preconditioning damage was not a major driver of landsliding here.

These results have significant implications for mass-wasting hazard and susceptibility modelling. First, as highlighted by Kirschbaum et al. [23], there remain large uncertainties in predicting how climate change may affect landsliding over the Himalaya. The results presented here contribute to reducing this uncertainty, as, when combined with possible ASM strength scenarios under future climate change conditions [51–55], our empirical relationship between ASM strength and mass-wasting can be used to provide quantitative assessments of expected changes in ASM-triggered mass-wasting across the Himalaya. Furthermore, if future climate change scenarios suggest an increase in the occurrence of 4 – 33 year return period rainfall events [56,57], then mass-wasting perturbations such as those in 1993 and 2002 will become more frequent, and thus contribute increasingly to long-term mass-wasting which becomes an increasingly pervasive hazard. Second, existing mass-wasting susceptibility models are typically time-independent, implicitly assuming that the conditions that produced past mass-wasting will remain the same in the future [58,59]. However, our results show that in active mountainous regions, earthquake preconditioning can cause transient, time-dependent mass-wasting perturbations. This suggests that post-earthquake rainfall-triggered landslide susceptibility modelling should account for the transient topographic signature of earthquakes. The finding that preconditioning is controlled by the product of PGA and excess topography is particularly useful, as it provides a framework for which preconditioning-induced mass-wasting can be modelled.

Methods

Mass-wasting mapping

Mass-wasting events were mapped using Landsat imagery. Landsat products were selected as they provide the longest continuously acquired space-based archive of the Earth's surface, and are the only product to contiguously cover Nepal over the 30-year time period we aimed to map. At the time of writing, Landsat imagery were freely available via the USGS Earth Explorer platform [60]. Mapping was conducted using Landsat 4/5 in years 1988 – 1999 and 2004 – 2010, Landsat 7 in years 2000 – 2003, and Landsat 8 in years 2013 – 2018. Landsat 7 could not be used for years 2004 – 2012 because Landsat 7 lost its scan-line corrector in 2003, with > 35% imagery data loss [61]. This was insufficient for mapping, so we reverted back to Landsat 4/5 imagery until Landsat 8 imagery became available in 2013. Consequently, 2011 and 2012 were not mapped as this period was only covered by Landsat 7 imagery. 2013 was mapped as normal using Landsat 8 pre-post monsoon imagery (i.e., landslides from 2011 and 2012 were fully discounted from the inventory, with only new landslides occurring post-2012 and pre-2014 mapped). Landsat products have a 16 day temporal resolution. However, in Nepal, with cloud cover pervasive throughout the year, pre- and post-ASM images were acquired between start October and end April, i.e., either side of the May – September monsoon-season. It should be noted that the post imagery used to map a given time slice was typically used as the pre-imagery for the next time slice, thus ensuring that mapping was continuous, with no significant time gaps. The name and date of the satellite imagery used to map each year, as well as a summary of each year's mass-wasting data, are shown in the Supplementary Materials (Table S1). Landsat 4/5 has a spatial resolution of 30 x 30 m, whilst Landsat 7/8 was pansharpened with panchromatic imagery to 15 x 15 m. Thus, the minimum mappable feature size was ~ 1000 m^2.

Mass-wasting features were identified by visual comparison between pre- and post-imagery for a given year. Images were viewed as false RGB images with Red band = Infrared, green band = green, and blue band = blue. This combination was used because the reflectivity differences strongly highlighted vegetated areas relative to bare earth. If a new bare-earth feature appeared in the landscape between the pre- and post-imagery and had the typical shape and location of a mass-wasting event it was delineated as a polygon. All types of rainfall-triggered landslides [62] were included in the inventory, i.e., landslides were not differentiated by type. Care was taken to avoid mapping features related to land clearance, such as deforestation and cut-and-fill practices, as well as features due to undercutting by roads or channels. All mapped mass-wasting events included the combined scar, runout and depositional zones, as these were not distinguishable at the spatial-resolution of the imagery. Steps were taken to avoid mass-wasting amalgamation, i.e. effort was made to separate mass-wasting events whose runouts combined to form one single deposit, as this is known to impact mapping results [63]. Mass-wasting events that scarred or disturbed vegetation/material within the boundary of a previous landslide were recorded as reactivations (failures involving the displacement of previously undisturbed material that initiated from or intersected with the boundary of a previous failure), although image resolution may mean some of these could have been remobilisations (movements of previously disturbed material only) rather than reactivations. In total, 12,920 moderate to large (~ 1000 m^2) mass-wasting events were mapped across 29 separate time slices from 1988 – 2018 (see Supplementary Data 1 for the geometric and satellite information of each mapped feature).

Each time slice included a given year's monsoon season (May – September) plus a varying number of non-monsoon months either side. The variation in the number of October – April months included in each time slice was an unavoidable consequence of the high levels of cloud cover across the Himalayas. However, as our time slices had varying lengths, both between time slices and within time slices (as several tiles were required to map the entire study region, and invariably these tiles had different acquisition dates and cloud cover), it is necessary to consider the effect of this on our results. Our analysis of ASM-triggered and extreme rainfall triggered mass-wasting assumes that all mass-wasting was triggered during a given time slice's monsoon season. As these time slices include months outside of the monsoon period, it is possible that some of these rainfall-triggered events did not occur during the monsoon. However, it is known that this region experiences little rainfall-triggered landsliding outside of the monsoon period [5,64]. Indeed, we find no correlation between the number of non-monsoon months within a time slice and number of mass-wasting events mapped (Supplementary Fig. S9). Furthermore, we find no correlation between the total rainfall in the non-monsoon months between time-slices and the deviation of a time-slice from the normalisation in Fig. 2b (Supplementary Fig. S10). This suggests, as expected, that variable time slice length cannot explain the normalisation results. To further ensure that errors in mapping procedure do not affect the results, we applied a 20% assumed error to all mapped mass-wasting areas. This assumed error should account for variability in mapped mass-wasting caused by including non-monsoon months, as well as for any erroneously included mass-wasting events that are attributable to non-rainfall dominated processes such as undercutting by river channels or earthquakes. Note that road-associated and coseismic mass-wasting events were explicitly not included in this inventory, though rainfall induced reactivations and remobilisations of coseismic mass-wasting are included. Coseismic mass-wasting events in 2015 were identified and avoided informed by the dataset of Roback et al.[24]. Furthermore, possible coseismic events triggered by an M_w 6.9 event that occurred midway through the 1988 monsoon season affecting a small portion of the study region were identified and avoided based on their slope position [65,66].

Scar-area and volume derivations

As outlined above, the satellite imagery resolution allowed mass-wasting features to be mapped with combined scar, runout and depositional zones. As total areas with long runouts can cause large overestimates in subsequent volume derivations, corrections for runout are needed by estimating landslide scar areas [3]. This was achieved using the procedure of Marc et al. [67]. First, mass-wasting widths were calculated for each mapped feature using their perimeters, areas and the assumption that each feature can be approximated by an elliptical shape [63,67]. Second, assuming that mass-wasting scars have an aspect ratio of 1.5, as found by Domej et al.[68] for a wide range of landslide sizes, scar areas can be calculated from $A_s = 1.5*W^2$, where A_s is scar area (m^2) and W is feature width (m).

Mass-wasting volumes were then estimated for both total areas and scar areas using the scaling relationships of Larsen et al. [28], $V = \alpha.A^\gamma$, where V is volume (m^3), A is area (m^2) and α and γ are constant scaling parameters. For scar areas, appropriate values for α and γ reported by Larsen et al. are: $\gamma = 1.262 \pm 0.009$ and $\log_{10}\alpha = -0.649 \pm 0.021$ for scar areas < 10,000 m^2 and

$\gamma = 1.41 \pm 0.02$ and $\log_{10}\alpha = -0.63 \pm 0.06$ for scar areas > 10,000 m^2. For total areas, we used the 'all landslide' parameters reported by Larsen et al., [28], where: $\gamma = 1.332 \pm 0.005$ and $\log_{10}\alpha = -0.836 \pm 0.015$. It should be noted that as these area-volume scaling relationships are designed for landslide events, they may overestimate the volumes of any remobilisations in our inventory, thus leading to potential overestimates in our overall "New + RR" rate. However, any errors should be accommodated by the 20% error applied to all mapped features and thus unlikely to impact the overall results.

Precipitation data

This paper use two precipitation products: PERSIANN-CDR and APHRODITE, with their product properties and use justifications outlined accordingly below.

The PERSIANN Climate Data Record (CDR) product has a spatial resolution of 0.25° by 0.25° and temporal resolution of 3 hours to 1 month over the period 1983 – present [29]. This record is developed using the PERSIANN algorithm on GridSat-B1 IR satellite data. This algorithm is trained using hourly stage IV precipitation data from the National Centres for Environmental Prediction (NCEP) and then adjusted using the Global Precipitation Climatology Project (GPCP) dataset [29]. This product was selected as it is one of only a few accessible precipitation products with a spatial resolution of at least 0.25° by 0.25° that fully spans our time period of 1988 – 2018 [30]. Daily precipitation totals (mm) for May – September were obtained from the CHRS data portal (https://chrsdata.eng.uci.edu/) [69] for our study region for all PERSIANN-CDR grid tiles that were at least 50% within our study region. Standard GIS tools were used to extract the various ASM strength metrics used throughout this paper.

PERSIANN-CDR is a widely used and comprehensively evaluated product (e.g. Nguyen et al., [70]). PERSIANN-CDR was found to perform excellently when evaluated against 1400 ground-stations at capturing the spatial and temporal patterns of rainfall in the monsoon-regions of eastern China [71], and outperformed the TMPA (TRMM Multi-satellite Precipitation Analysis) dataset in its ability to capture the overall characteristics of Hurricane Catrina [70]. Furthermore, PERSIANN-CDR was found to have lower monthly mean variance compared to other satellite products, showing particularly small variance with the GPCP1DD product [72,73]. Similarly, despite being slightly outperformed by other products, the PERSIANN-CDR data set was capable of capturing inter-annual monsoon precipitation in Pakistan, with high (0.8) R values when compared to in-situ data [74]. However, PERSIANN-CDR has some limitations. First, as with all satellite products, it can struggle to capture orographic effects [75]. However, a benefit of PERSIANN-CDR is that it is designed specifically for use in longer-term studies [29,76] and is considered one of the most temporally homogenous products. As such, unlike other satellite products whose methodologies could introduce temporal variance, any errors in the PERSIANN-CDR product introduced by orographic effects should be more systematic through time, and so not significantly bias our time-series. This is important for this study, which requires a homogenous rainfall series to ensure that any normalised perturbations are due to physical process changes, rather than changes in rainfall data collection methodology. Second, PERSIANN-CDR is reported to have a tendency to under-predict values of extreme precipitation [71,76]. Thus, to ensure that any under prediction of rainfall by PERSIANN-CDR does not impact our normalisation, and to allow for a more robust consideration of daily extreme precipitation, we also make use of the APHRODITE product [31].

APHRODITE (Asian Precipitation—Highly Resolved Observational Data Integration Towards Evaluation of water resources) has the same spatial resolution as PERSIANN-CDR

(0.25° by 0.25°) across monsoon-Asia, with daily coverage across the study region for 1951 – 2015. APHRODITE is based on rain gauge data from 5,000–12,000 stations and is designed to optimise representation of orographic precipitation patterns. The temporal coverage of APHRODITE has advantages and disadvantages for this study. The disadvantage is that it does not allow us to assess the post-2015 earthquake preconditioning (a key aim of the study,, and why the PERSIANN-CDR data were used to assess the entire time series). The advantage of the temporal coverage is that with a 64-year time-series, robust analysis of extreme events and recurrence intervals are possible. APHRODITE is also considered as one of the most accurate products over the Himalayas [31,77], making it a good product to corroborate the results of our normalisation undertaken with PERSIANN-CDR. In summary, PERSIANN-CDR is used obtain a time-stable assessment of the entire time series, including the key post-2015 period (which APHRODITE cannot give without blending it with another dataset), whilst APHRODITE is used to corroborate the PERSIANN-CDR data and provide an unbiased comparison between the ASM-strength analysis and extreme daily rainfall analysis.

ASM strength-normalised mass-wasting rate

Empirical relationships between ASM strength and mass-wasting can be used to predict how much background mass-wasting is expected to occur each year based on that years ASM strength. Four previously investigated proxies of ASM strength[3,32], for both the PERSIANN-CDR and APHRODITE data, were correlated with each measure of mass-wasting volume (total and scar volumes (m^3/km^2) of new and reactivated/remobilised landslides ["New + RR"] and of only new landslides ["New Only"]). These proxies were: total grid-averaged MJJAS precipitation, total grid-averaged MJJAS precipitation > 25 mm, total grid-averaged precipitation from 15th June – September, and total grid-averaged precipitation > 25 mm for 15th June – September. The ASM strength proxies which provided the best fit to the mass-wasting data were total MJJAS rainfall for the PERSIANN-CDR data, and total MJJAS rainfall > 0.25 mm for the APHRODITE data (see Fig. 2 for best fit results and Supplementary Figs. S1 - 3 for all other correlations).

For each measure, the ASM strength-normalised rate for each year is then calculated by taking the ratio of the actual mass-wasting mapped for that year to that predicted by the equations in Figure 2. A value of one indicates that the actual observed mass-wasting in a year is what would be expected given the ASM strength, whilst a value significantly above one indicates that there was more mass-wasting than expected given the ASM strength, implying perturbation above the background by some other event. Errors in the normalised rate include the standard error in the data points used to calculate the prediction equations, an assumed standard deviation of 20% in mass wasting area to account for variability in mapping period and any mapping error, and the standard deviations reported in the area-volume conversion parameters. Assuming that these errors are uncorrelated, they were combined using standard Gaussian propagation of error to obtain the uncertainties for each measure (Fig. 3a – b).

Furthermore, prior to correlating mass-wasting with ASM strength, we removed the largest landslide from a given monsoon season if it had a scar-volume twice as large as the second largest landslide. This follows Marc et al.,[3] and is designed to remove any landslides that are anomalously large for the monsoon-season in which they occurred, and thus likely caused by progressive failure across multiple monsoon-seasons (e.g., the Jure landslide [34,3]). By removing these events, we can be confident that any identified perturbations are not due to a single anomalously large landslide. In total, 12 events were removed from the analysis, one event in each of 1988, 1996, 2000, 2003, 2004, 2005, 2014 and 2017, and two events in both 2009 and 2015.

Three-parameter inverse-gamma distributions

To further confirm that the identified perturbations are not due to stochastic variation in landslide size, we fit three-parameter inverse gamma distributions to the probability density functions (PDF) of landslide area for several subsets of our inventory (all years, all pre-2015 non-perturbed years, 1989, 1993, 1995, 2002, 2015 and 2016 – 2018). The PDF of landslide area p (AL), is given by equation 1 [43]:

$$p(A_L) = \frac{1}{N_{LT}}\frac{\partial N_L}{\partial A_L} \qquad \text{Equation 1}$$

Where N_{LT} is the total number of landslides in the subset, A_L is landslide area, δN_L is the number of landslides with areas between A_L and $A_L + \delta A_L$. The three-parameter inverse-gamma distribution fitted to the PDFs is defined by equation 2 [43]:

$$pdf\ (A_l|\alpha,\eta,\lambda) = \left[\frac{\lambda^{2\alpha}}{\Gamma(\alpha)}\right]\left[\left(\frac{1}{x+\eta^2}\right)^{(\alpha+1)}\right] exp\left[-\frac{\lambda^2}{x+\eta^2}\right] \qquad \text{Equation 2}$$

Where α controls the exponent of the inverse-power law (i.e., the steepness of the right tail of the probability density function), η controls the steepness, or bend, of the left tail of the probability density function, and λ controls the position of the rollover. The position of the rollover indicates the landslide area below which the inverse power-law decay observed for medium and larger landslides no longer applies. The PDFs and three-parameter inverse gamma distribution were fitted to each subset using Landsat software (version 10)[78], which utilises Maximum Likelihood Estimation (MLE) to optimise the parameters of the probability density function and a bootstrapped (here with 1000 simulations) Kolmogorov-Smirnov (K-S) test to estimate parameter uncertainty and overall goodness of fit of the inventory data to the fitted distribution.

The exponent, α, of the inverse power-law describes the rate at which the probability of getting larger landslides decreases. A larger exponent indicates that the probability of getting larger events is decreasing quickly, and thus that larger landslides are contributing less to each inventory. Conversely, a smaller exponent indicates that the probability of getting larger events is decreasing more slowly, and thus that larger landslides are contributing more to each inventory. Thus, if the exponents of the distributions fitted to each subset are similar above comparable cut-offs, then we can be confident that a perturbation is caused by some physical process that causes an increase in landslides of all sizes, rather than a small number of anomalously large landslide events.

Note that our rollover values (see main text) are larger than the values obtained for the Gorkha coseismic landslides (2500 m^2) [24] and monsoon-triggered landslides mapped by Marc et al. (1200 m^2) [3]. This is likely because of differences in mapping resolution, with the minimum possible size feature that could be mapped by Roback et al. [24] and Marc et al. [3] an order of magnitude smaller than could be mapped here. However, our rollover values are comparable to similar studies using imagery with 30 – 15 m resolution imagery [79], suggesting that our inventory is as substantially complete as would be expected given the resolution of the satellite imagery. Our scaling exponents are also slightly smaller than the value of ~2.47 obtained for higher resolution inventories of both monsoon-triggered and earthquake-triggered landslides in Nepal [3,24]. Again, this is likely an artefact of imagery resolution, and the fact that we are under-sampling the smallest events.

Percentage change in mass-wasting

To calculate the percentage change in 2015 mass-wasting, we divided the study region into 84 grid cells (Fig. 6). For each grid-cell, we calculated the mean mass-wasting (based on scar volumes) observed across all unperturbed monsoon-seasons (i.e., all years except 1988, 1989, 1993, 1995, 2002 and 2015). We then calculated the percentage change in 2015 monsoon-triggered mass-wasting for each grid relative to that grid's mean. By only calculating each cell's average with the non-perturbed years, we obtain an approximation of average mass-wasting expected per grid in a typical monsoon season without extreme rainfall. As such, whilst this does not consider monsoonal forcing in the detail it was on the regional scale, as we know that 2015 was not impacted by any extreme rainfall, each grid's 2015 percentage change in monsoon-triggered mass-wasting should approximately reflect the "above average" or excess mass-wasting experienced in 2015 due to the earthquake compared to an average non-perturbed monsoon season.

Excess Topography

Excess topography, a measure of the total volume of rock mass above a specified threshold hillslope angle [47], was extracted from the Japanese Aerospace Exploration Agency (JAXA)-copyrighted ALOS World 3D DEM using the "excesstopography" function in the Matlab TopoToolbox [80]. Excess topography was calculated at five threshold angles: 25°, 30°, 35°, 40° and 45°. The average excess topography at each threshold across each grid-cell was then extracted using standard ArcGIS zonal statistics tools.

Acknowledgments

This work was supported by the Natural Environment Research Council through the EnvEast Doctoral Training Partnership [NE/L002582/1] with CASE-funding from AECOM. We would also like to thank the editor, Sebastian Mueller, and reviewers, Oliver Francis and Marc Odin and an anonymous reviewer for their constructive and useful comments that have improved this paper.

Author Contributions

SB and MW conceived the study with input from MS and GB. JJ performed mapping and analysis of mass-wasting data with input from SB, GB, MS and MW. JJ, SB and MW conducted field validation. JJ wrote the manuscript with contributions from SB, GB, MS and MW.

Data Availability

The raw mass-wasting data used within this manuscript is provided as a .text file (Supplementary Data 1) that includes the geometries (areas, volumes), centroid coordinates and satellite data used to map each individual feature.

Code Availability

This manuscript includes no custom code or algorithms.

Competing Interest Statement

The authors declare no competing interests.

References

1. Bennett, G. L., Miller, S. R., Roering, J. J. & Schmidt, D. A. Landslides, threshold slopes, and the survival of relict terrain in the wake of the Mendocino Triple Junction. *Geology* **44**, 363–366 (2016).

2. Morin, G. P. *et al.* Annual Sediment Transport Dynamics in the Narayani Basin, Central Nepal: Assessing the Impacts of Erosion Processes in the Annual Sediment Budget. *J. Geophys. Res. Earth Surf.* **123**, 2341–2376 (2018).

3. Marc, O. *et al.* Long-term erosion of the Nepal Himalayas by bedrock landsliding: the role of monsoons, earthquakes and giant landslides. *Earth Surf. Dyn.* **7**, 107–128 (2019).

4. Froude, M. J. & Petley, D. N. Global fatal landslide occurrence from 2004 to 2016. *Nat. Hazards Earth Syst. Sci.* **18**, 2161–2181 (2018).

5. Petley, D. N. *et al.* Trends in landslide occurrence in Nepal. *Nat Hazards* **43**, 23–44 (2007).

6. Larsen, I. J. & Montgomery, D. R. Landslide erosion coupled to tectonics and river incision. *Nat. Geosci.* **5**, 468–473 (2012).

7. Bennett, G. L. *et al.* Historic drought puts the brakes on earthflows in Northern California. *Geophys. Res. Lett.* **43**, 5725–5731 (2016).

8. Marshall, J. A. *et al.* Frost for the Trees: Did climate increase erosion in unglaciated landscapes during the late Pleistocene? *Sci. Adv.* **1**, 1–10 (2015).

9. Rahaman, W., Singh, S. K., Sinha, R. & Tandon, S. K. Climate control on erosion distribution over the Himalaya during the past ~ 100 ka. *Geology* **37**, 559–562 (2009).

10. Molnar, P. & England, P. Late Cenozoic uplift of mountain ranges and global climate change:

Chicken or egg? *Nature* **346**, 29–34 (1990).

11. Wolman, M. G. & Miller, J. P. Magnitude and Frequency of Forces in Geomorphic Processes. *J. Geol.* **68**, 54–74 (1960).

12. Rathburn, S. L. *et al.* The fate of sediment, wood, and organic carbon eroded during an extreme flood, Colorado Front Range, USA. *Geology* **45**, 499–502 (2017).

13. Chen, C. *et al.* The impact of storm-triggered landslides on sediment dynamics and catchment-wide denudation rates in the southern Central Range of Taiwan following the extreme rainfall event of Typhoon Morakot. *Earth Surf. Process. Landforms* esp.4753 (2020). doi:10.1002/esp.4753

14. Dadson, S. J. *et al.* Earthquake-triggered increase in sediment delivery from an active mountain belt. *Geology* **32**, 733–736 (2004).

15. Andermann, C., Crave, A., Gloaguen, R., Davy, P. & Bonnet, S. Connecting source and transport: Suspended sediments in the Nepal Himalayas. *Earth Planet. Sci. Lett.* **351**–**352**, 158–170 (2012).

16. Kirchner, J. W. *et al.* Mountain erosion over 10 yr, 10 k.y., and 10 m.y. time scales. *Geology* **29**, 591–594 (2001).

17. Marc, O., Hovius, N., Meunier, P., Uchida, T. & Hayashi, S. Transient changes of landslide rates after earthquakes. *Geology* **43**, 883–886 (2015).

18. Struck, M. *et al.* Monsoonal hillslope processes determine grain size-specific suspended sediment fluxes in a trans-Himalayan river. *Geophys. Res. Lett.* **42**, 2302–2308 (2015).

19. Bookhagen, B., Thiede, R. C. & Strecker, M. R. Abnormal monsoon years and their control on erosion and sediment flux in the high, arid northwest Himalaya. *Earth Planet. Sci. Lett.* **231**, 131–146 (2005).

20. Dahal, R. K. & Hasegawa, S. Representative rainfall thresholds for landslides in the Nepal

Himalaya. *Geomorphology* **100**, 429–443 (2008).

21. Cook, K. L., Andermann, C., Gimbert, F., Adhikari, B. R. & Hovius, N. Glacial lake outburst floods as drivers of fluvial erosion in the Himalaya. *Science.* **362**, 53–57 (2018).

22. Dhital, M. R. Causes and consequences of the 1993 debris flows and landslides in the Kulekhani watershed, central Nepal. in *Proc. 3rd Intl. Conf. Debris-Flow Hazards Mitigation: Mechanics, Prediction and Assessment* (eds. Rickenmann, D. & Chen, C. L.) **2**, 931–942 (Millpress, Rotterdam, 2003).

23. Kirschbaum, D., Kapnick, S. B., Stanley, T. & Pascale, S. Changes in Extreme Precipitation and Landslides Over High Mountain Asia. *Geophys. Res. Lett.* **47**, (2020).

24. Roback, K. *et al.* The size, distribution, and mobility of landslides caused by the 2015 Mw7.8 Gorkha earthquake, Nepal. *Geomorphology* **301**, 121–138 (2018).

25. Burbank, D. W., Bookhagen, B., Gabet, E. J. & Putkonen, J. Modern climate and erosion in the Himalaya. *Comptes Rendus - Geoscience* **344**, 610–626 (2012).

26. Martha, T. R., Roy, P., Mazumdar, R., Govindharaj, K. B. & Kumar, K. V. Spatial characteristics of landslides triggered by the 2015 Mw 7.8 (Gorkha) and Mw 7.3 (Dolakha) earthquakes in Nepal. *Landslides* **14**, 697–704 (2017).

27. Parker, R. N. *et al.* Spatial distributions of earthquake-induced landslides and hillslope preconditioning in the northwest South Island, New Zealand. *Earth Surf. Dynam* **3**, 501–525 (2015).

28. Larsen, I. J., Montgomery, D. R. & Korup, O. Landslide erosion controlled by hillslope material. *Nat. Geosci.* **3**, 247–251 (2010).

29. Ashouri, H. *et al.* PERSIANN-CDR: Daily Precipitation Climate Data Record from Multisatellite Observations for Hydrological and Climate Studies. *Bull. Am. Meteorol. Soc.* **96**, 69–83 (2015).

30. Sun, Q. *et al.* A Review of Global Precipitation Data Sets: Data Sources, Estimation, and Intercomparisons. *Rev. Geophys.* **56**, 79–107 (2018).

31. Yatagai, A. *et al.* Aphrodite constructing a long-term daily gridded precipitation dataset for Asia based on a dense network of rain gauges. *Bull. Am. Meteorol. Soc.* **93**, 1401–1415 (2012).

32. Muñoz-Torrero Manchado, A. *et al.* Three decades of landslide activity in western Nepal: new insights into trends and climate drivers. *Landslides* (2021). doi:10.1007/s10346-021-01632-6

33. Li, J. & Zeng, Q. A unified monsoon index. *Geophys. Res. Lett.* **29**, 115–1 (2002).

34. Yagi, H. *et al.* Slope Deformation caused Jure Landslide 2014 Along Sun Koshi in Lesser Nepal Himalaya and Effect of Gorkha Earthquake 2015. in *Workshop on World Landslide Forum WLF 2020: Understanding and Reducing Landslide Disaster Risk* 65–72 (Springer, Cham, 2021). doi:10.1007/978-3-030-60319-9_5

35. Paudel, P. P., Omura, H., Kubota, T. & Morita, K. Landslide damage and disaster management system in Nepal. *Disaster Prev. Manag. An Int. J.* **12**, 413–419 (2003).

36. Jain, V. K., Pandey, R. P., Jain, M. K. & Byun, H. R. Comparison of drought indices for appraisal of drought characteristics in the Ken River Basin. *Weather Clim. Extrem.* **8**, 1–11 (2015).

37. Wu, H., Hayes, M. J., Weiss, A. & Hu, Q. An evolution of the standardized precipitation index, the China-Z index and the statistical Z-score. *Int. J. Climatol.* **21**, 745–758 (2001).

38. Gabet, E. J., Burbank, D. W., Putkonen, J. K., Pratt-Sitaula, B. A. & Ojha, T. Rainfall thresholds for landsliding in the Himalayas of Nepal. *Geomorphology* **63**, 131–143 (2004).

39. Gruber, S. Derivation and analysis of a high-resolution estimate of global permafrost zonation. *Cryosph.* **6**, 221–233 (2012).

40. Rathburn, S. L., Shahverdian, S. M. & Ryan, S. E. Post-disturbance sediment recovery: Implications for watershed resilience. *Geomorphology* **305**, 61–75 (2018).

41. Hovius, N. *et al.* Prolonged seismically induced erosion and the mass balance of a large earthquake. *Earth Planet. Sci. Lett.* **304**, 347–355 (2011).

42. Dahlquist, M. P. & West, A. J. Initiation and Runout of Post-Seismic Debris Flows: Insights From the 2015 Gorkha Earthquake. *Geophys. Res. Lett.* **46**, 9658–9668 (2019).

43. Malamud, B. D., Turcotte, D. L., Guzzetti, F. & Reichenbach, P. Landslides, earthquakes, and erosion. *Earth Planet. Sci. Lett.* **229**, 45–59 (2004).

44. Wald, D. J. & Allen, T. I. Topographic slope as a proxy for seismic site conditions and amplification. *Bulletin of the Seismological Society of America* **97**, 1379–1395 (2007).

45. Paolucci, R. Amplification of earthquake ground motion by steep topographic irregularities. *Earthq. Eng. Struct. Dyn.* **31**, 1831–1853 (2002).

46. Nguyen, K. Van & Gatmiri, B. Evaluation of seismic ground motion induced by topographic irregularity. *Soil Dyn. Earthq. Eng.* **27**, 183–188 (2007).

47. Blöthe, J. H., Korup, O. & Schwanghart, W. Large landslides lie low: Excess topography in the Himalaya-Karakoram ranges. *Geology* **43**, 523–526 (2015).

48. Meunier, P., Hovius, N. & Haines, A. J. Regional patterns of earthquake-triggered landslides and their relation to ground motion. *Geophys. Res. Lett.* **34**, L20408 (2007).

49. Yuan, R. M. *et al.* Density distribution of landslides triggered by the 2008 Wenchuan earthquake and their relationships to peak ground acceleration. *Bull. Seismol. Soc. Am.* **103**, 2344–2355 (2013).

50. Marc, O. *et al.* Initial insights from a global database of rainfall-induced landslide inventories: the weak influence of slope and strong influence of total storm rainfall. *Earth Surf. Dyn.* **6**, 903–922 (2018).

51. Douville, H. *et al.* Impact of CO2 Doubling on the Asian Summer Monsoon. *J. Meteorol. Soc. Japan. Ser. II* **78**, 421–439 (2000).

52. Hu, Z.-Z., Latif, M., Roeckner, E. & Bengtsson, L. Intensified Asian Summer Monsoon and its variability in a coupled model forced by increasing greenhouse gas concentrations. *Geophys. Res. Lett.* **27**, 2681–2684 (2000).

53. May, W. Simulated changes of the Indian summer monsoon under enhanced greenhouse gas conditions in a global time-slice experiment. *Geophys. Res. Lett.* **29**, 1118 (2002).

54. Annamalai, H., Hamilton, K. & Sperber, K. R. The South Asian summer monsoon and its relationship with ENSO in the IPCC AR4 simulations. *J. Clim.* **20**, 1071–1092 (2007).

55. Turner, A. G. & Annamalai, H. Climate change and the South Asian summer monsoon. *Nature Climate Change* **2**, 587–595 (2012).

56. Kripalani, R. H., Oh, J. H., Kulkarni, A., Sabade, S. S. & Chaudhari, H. S. South Asian summer monsoon precipitation variability: Coupled climate model simulations and projections under IPCC AR4. *Theor. Appl. Climatol.* **90**, 133–159 (2007).

57. Karki, R., Hasson, S. ul, Schickhoff, U., Scholten, T. & Böhner, J. Rising Precipitation Extremes across Nepal. *Climate* **5**, 4 (2017).

58. Guzzetti, F., Carrara, A., Cardinali, M. & Reichenbach, P. Landslide hazard evaluation: a review of current techniques and their application in a multi-scale study, Central Italy. *Geomorphology* **31**, 181–216 (1999).

59. Reichenbach, P., Rossi, M., Malamud, B. D., Mihir, M. & Guzzetti, F. A review of statistically-based landslide susceptibility models. *Earth-Science Rev.* **180**, 60–91 (2018).

60. Woodcock, C. E. *et al.* Free access to Landsat imagery. *Science* **320**, 1011 (2008).

61. Alexandridis, T. K. *et al.* Rapid error assessment for quantitative estimations from Landsat 7 gap-filled images. *Remote Sens. Lett.* **4**, 920–928 (2013).

62. Varnes, D. J. Slope movement types and processes. *Spec. Rep.* **176**, 11–33 (1978).

63. Marc, O. & Hovius, N. Amalgamation in landslide maps: effects and automatic detection. *Nat.*

Hazards Earth Syst. Sci. **15**, 723–733 (2015).

64. Stanley, T., Kirschbaum, D. B., Pascale, S. & Kapnick, S. Extreme precipitation in the Himalayan landslide hotspot. in *Advances in Global Change Research* **69**, 1087–1111 (Springer, 2020).

65. Densmore, A. L. & Hovius, N. Topographic fingerprints of bedrock landslides. *Geology* **28**, 371–374 (2000).

66. Meunier, P., Hovius, N. & Haines, J. A. Topographic site effects and the location of earthquake induced landslides. *Earth Planet. Sci. Lett.* **275**, 221–232 (2008).

67. Marc, O. *et al.* Initial insights from a global database of rainfall-induced landslide inventories: the weak influence of slope and strong influence of total storm rainfall. *Earth Surf. Dyn.* **6**, 903–922 (2018).

68. Domej, G., Bourdeau, C., Lenti, L., Martino, S. & Piuta, K. Mean landslide geometries inferred from a global database of earthquake- and non-earthquake-triggered landslides. *Ital. J. Eng. Geol. Environ.* **2**, 87–107 (2017).

69. Nguyen, P. *et al.* The CHRS data portal, an easily accessible public repository for PERSIANN global satellite precipitation data. *Sci. Data* **6**, (2019).

70. Nguyen, P. *et al.* PERSIANN-CDR for hydrology and hydro-climatic applications. in *Advances in Global Change Research* **69**, 993–1012 (Springer, 2020).

71. Miao, C., Ashouri, H., Hsu, K.-L., Sorooshian, S. & Duan, Q. Evaluation of the PERSIANN-CDR Daily Rainfall Estimates in Capturing the Behavior of Extreme Precipitation Events over China. *J. Hydrometeorol.* **16**, 1387–1396 (2015).

72. Gehne, M., Hamill, T. M., Kiladis, G. N. & Trenberth, K. E. Comparison of global precipitation estimates across a range of temporal and spatial scales. *J. Clim.* **29**, 7773–7795 (2016).

73. Huffman, G. J. *et al.* Global precipitation at one-degree daily resolution from multisatellite observations. *J. Hydrometeorol.* **2**, 36–50 (2001).

74. Ullah, W. *et al.* Comparing Multiple Precipitation Products against In-Situ Observations over Different Climate Regions of Pakistan. *Remote Sens.* **11**, 628 (2019).

75. Adam, J. C., Clark, E. A., Lettenmaier, D. P. & Wood, E. F. Correction of global precipitation products for orographic effects. *J. Clim.* **19**, 15–38 (2006).

76. Beck, H. E. *et al.* Global-scale evaluation of 22 precipitation datasets using gauge observations and hydrological modeling. *Hydrol. Earth Syst. Sci.* **21**, 6201–6217 (2017).

77. Andermann, C., Bonnet, S. & Gloaguen, R. Evaluation of precipitation data sets along the Himalayan front. *Geochemistry, Geophys. Geosystems* **12**, n/a-n/a (2011).

78. Rossi, M. & Malamud, B. D. *LAMPRE, Prototype SW for determination of landslide statistics from inventory maps*. (2014).

79. Tanyaş, H., Westen, C. J., Allstadt, K. E. & Jibson, R. W. Factors controlling landslide frequency–area distributions. *Earth Surf. Process. Landforms* **44**, 900–917 (2019).

80. Schwanghart, W. & Kuhn, N. J. TopoToolbox: A set of Matlab functions for topographic analysis. *Environ. Model. Softw.* **25**, 770–781 (2010).

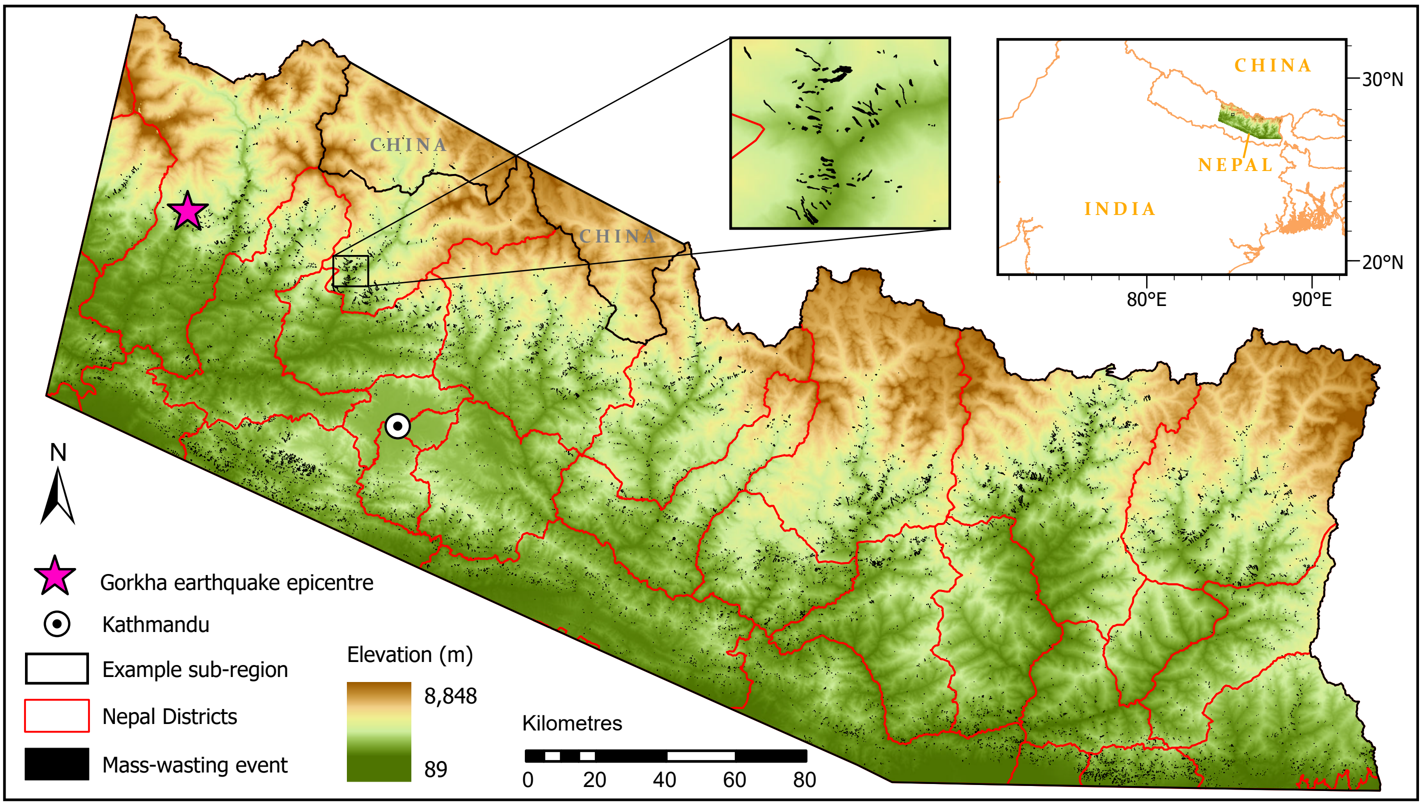

Figure 1. Location of our study region and all 12,290 mapped monsoon-triggered mass-wasting features, including a detailed view of a smaller sub-region demonstrating the detail of the mapped polygons. Also shown are the outlines of all Nepal Districts within the study region, including Kathmandu city and Gorkha earthquake epicentre locations. Elevation data is derived from the ALOS World 3D (AW3D30) DEM developed by and copyrighted to the Japanese Aerospace Exploration Agency (JAXA).

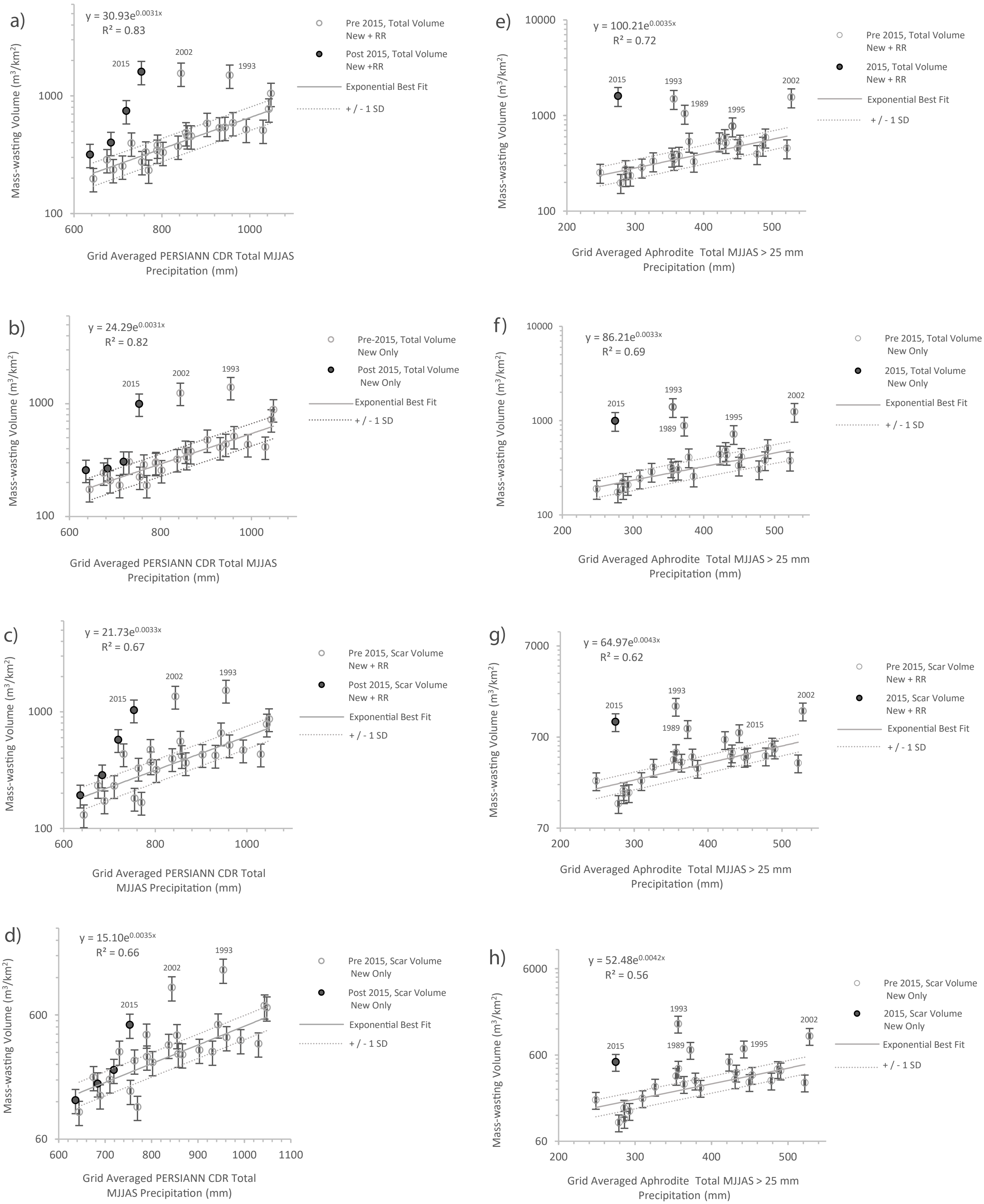

a)
y = 30.93e0.0031x
R² = 0.83
Pre 2015, Total Volume New + RR
Post 2015, Total Volume New +RR
Exponential Best Fit
+ / - 1 SD
2015
2002
1993
Mass-wasting Volume (m3/km2)
Grid Averaged PERSIANN CDR Total MJJAS Precipitation (mm)
b)
y = 24.29e0.0031x
R² = 0.82
Pre-2015, Total Volume New Only
Post 2015, Total Volume New Only
Exponential Best Fit
+ / - 1 SD
2015
2002
1993
Mass-wasting Volume (m3/km2)
Grid Averaged PERSIANN CDR Total MJJAS Precipitation (mm)
c)
y = 21.73e0.0033x
R² = 0.67
Pre 2015, Scar Volume New + RR
Post 2015, Scar Volume New + RR
Exponential Best Fit
+ / - 1 SD
2015
2002
1993
Mass-wasting Volume (m3/km2)
Grid Averaged PERSIANN CDR Total MJJAS Precipitation (mm)
d)
y = 15.10e0.0035x
R² = 0.66
Pre 2015, Scar Volume New Only
Post 2015, Scar Volume New Only
Exponential Best Fit
+ / - 1 SD
2015
2002
1993
Mass-wasting Volume (m3/km2)
Grid Averaged PERSIANN CDR Total MJJAS Precipitation (mm)
e)
y = 100.21e0.0035x
R² = 0.72
Pre 2015, Total Volume New + RR
2015, Total Volume New + RR
Exponential Best Fit
+ / - 1 SD
2015
1993
1989
1995
2002
Mass-wasting Volume (m3/km2)
Grid Averaged Aphrodite Total MJJAS > 25 mm Precipitation (mm)
f)
y = 86.21e0.0033x
R² = 0.69
Pre 2015, Total Volume New Only
2015, Total Volume New Only
Exponential Best Fit
+ / - 1 SD
2015
1993
1989
1995
2002
Mass-wasting Volume (m3/km2)
Grid Averaged Aphrodite Total MJJAS > 25 mm Precipitation (mm)
g)
y = 64.97e0.0043x
R² = 0.62
Pre 2015, Scar Volme New + RR
2015, Scar Volume New + RR
Exponential Best Fit
+ / - 1 SD
2015
1993
1989
2015
2002
Mass-wasting Volume (m3/km2)
Grid Averaged Aphrodite Total MJJAS > 25 mm Precipitation (mm)
h)
y = 52.48e0.0042x
R² = 0.56
Pre 2015, Scar Volume New Only
2015, Scar Volume New Only
Exponential Best Fit
+ / - 1 SD
2015
1993
1989
1995
2002
Mass-wasting Volume (m3/km2)
Grid Averaged Aphrodite Total MJJAS > 25 mm Precipitation (mm)

Figure 2 (above). a – d) Empirical relationships between measures of mass-wasting volume (m^3/km^2) and PERSIANN-CDR total MJJAS precipitation for a) total "New + RR" volume, b) total "New Only" volume, c) scar "New + RR" volume and d) scar "New Only" volume. e – h) Empirical relationships between measures of mass-wasting volume (m^3/km^2) and APHRODITE total MJJAS precipitation > 25 mm for e) total "New + RR" volume, f) total "New Only" volume, g) scar "New + RR" volume and h) scar "New Only" volume. Where, in all cases "New + RR" refers to the combined volumes of both new failures and reactivations/remobilisations and "New Only" refers to just the volumes of new failures, with reactivations and remobilisations excluded. The exponential best fits shown on these graphs apply to the non-anomalous pre-2015 points only, with all anomalous points labelled individually. The post-2015 points are also shown for reference, as are the +/- 1 standard errors on the best-fit equations.

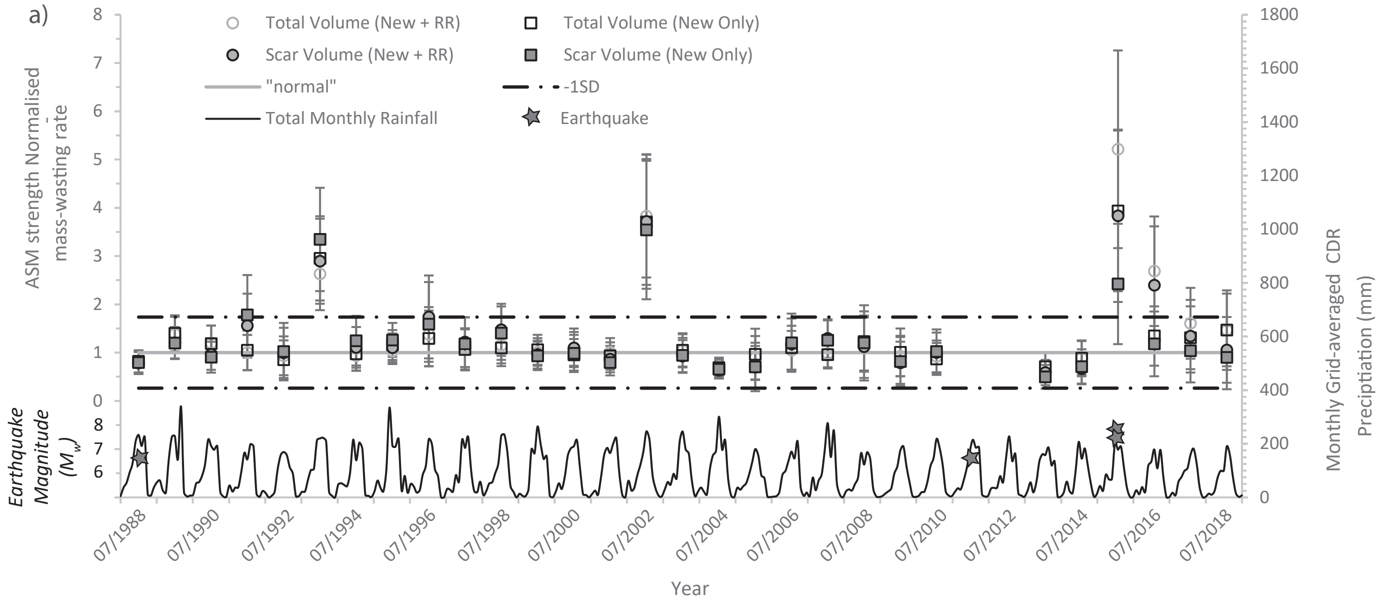

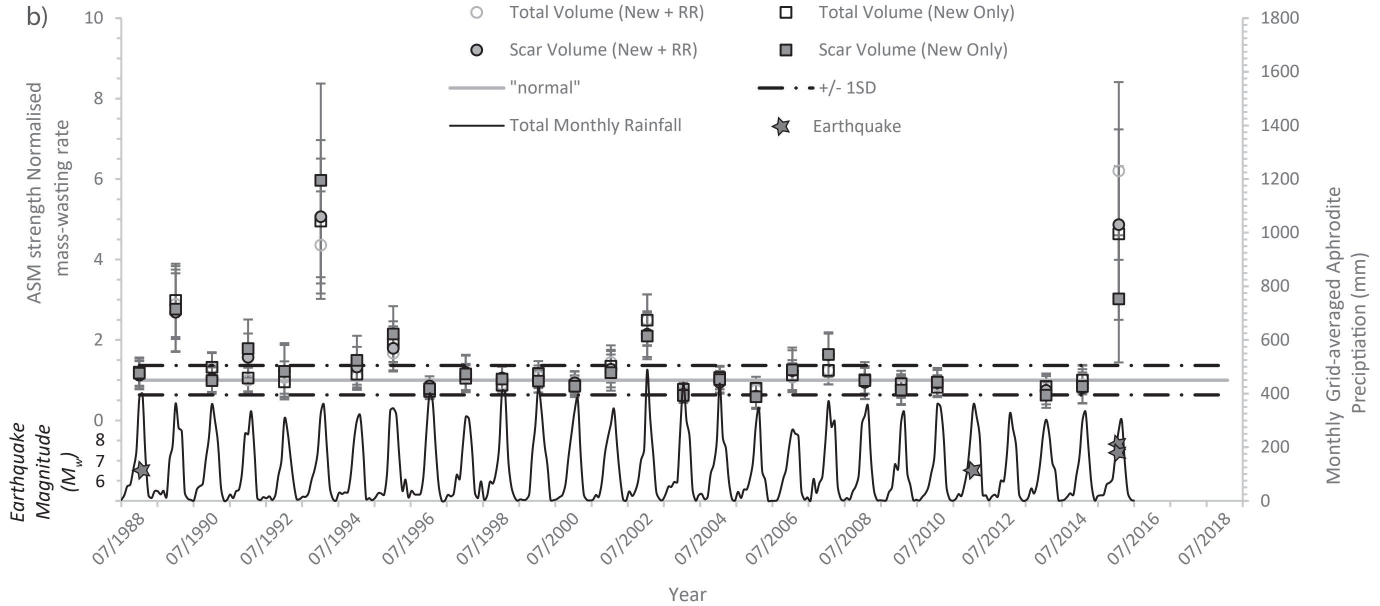

Figure 3. ASM strength-normalised rate of mass-wasting between 1988 and 2018 for a) the normalisation using the PERSIANN-CDR data and total MJJAS precipitation, and b) the normalisation using the APHRODITE data and total MJJAS precipitation > 25 mm. In both cases, most years fall within a narrow window around the normal, with perturbations in 1993, 2002 and 2015 in a), and 1989, 1993, 1995, 2002 and 2015 in b). The occurrences of historical $M_w > 6.0$ earthquakes are also shown. Also shown are the monthly grid-averaged PERSIANN-CDR (a) and APHRODITE (b) precipitation totals across the study region between 1988 and 2018. The errors in the normalised rate include the standard error in the data points used to calculate the prediction equations in Fig. 2, an assumed standard deviation of 20% on the mapped mass-wasting feature areas, and the standard deviations reported in Larsen et al. [28] area-volume conversion parameters. On the assumption that these errors are uncorrelated, they were combined using standard Gaussian propagation to obtain the final error bar uncertainties.

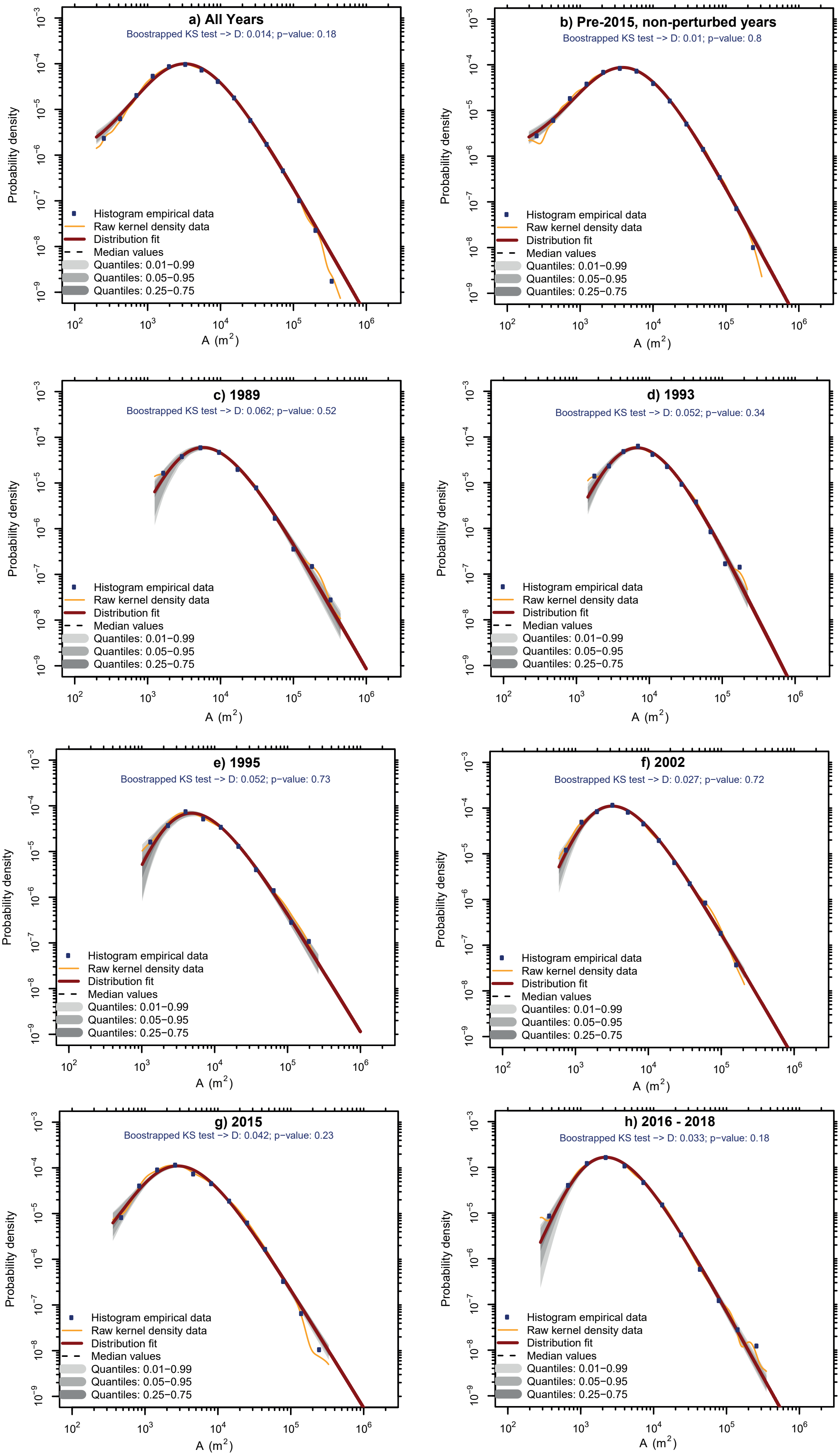

Figure 4. Probability Density Functions (PDFs) of landslide area fitted with inverse-gamma power law distributions for a) all years, b) the pre-2015 non-perturbed years, c) 1989, d) 1993, e) 1995, f) 2002, g) 2015, h post-2015). All PDFs and fitted distributions were calculated and plotted using the Landsat Software (version 10).

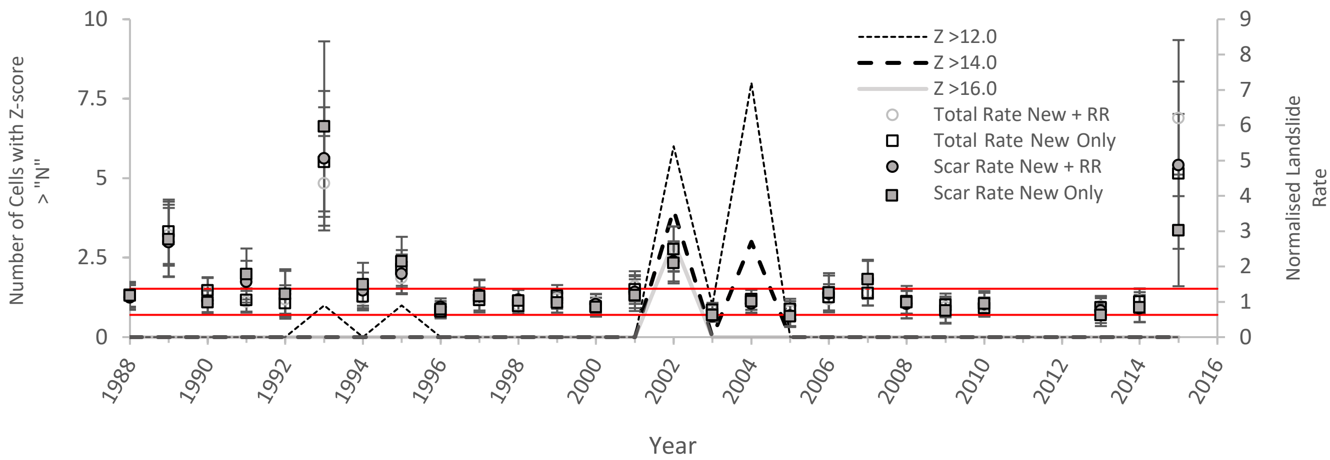

Figure 5. Number of daily cells per monsoon season that had Z-score anomalies greater than 12, 14 and 16. For reference, the normalised rates and associated +/- 1 SD (red lines) from Fig. 3b are also shown.

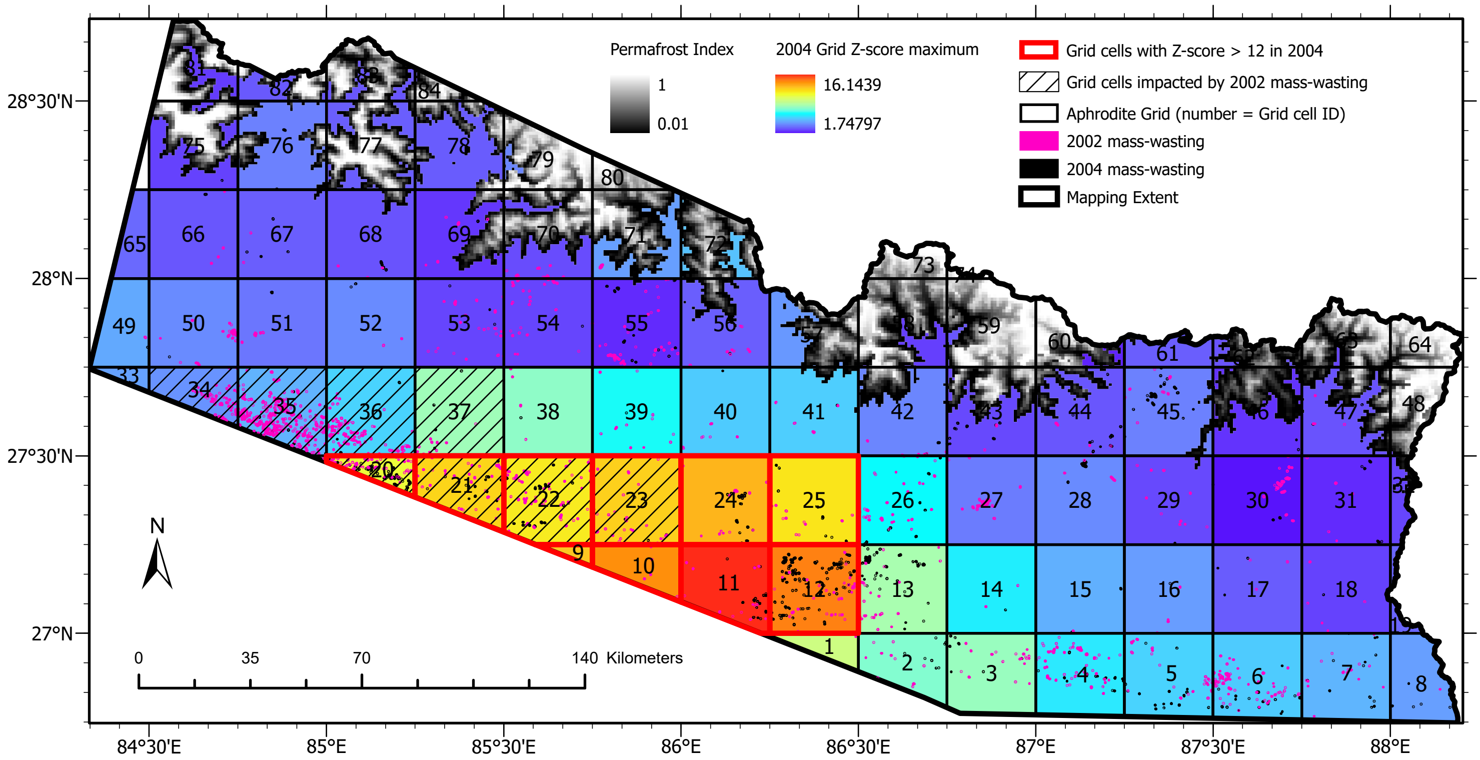

Figure 6. The locations and IDs of the 84 APHRODITE rainfall grid-cells across the study region. Maximum Z-scores from the 2004 monsoon seasons are shown alongside the 2004 mass-wasting. Also shown is the extent of the 2002 extreme rainfall, the mass-wasting from 2002 and the extent of permafrost, as defined by Gruber (2012) [39], across the study region.

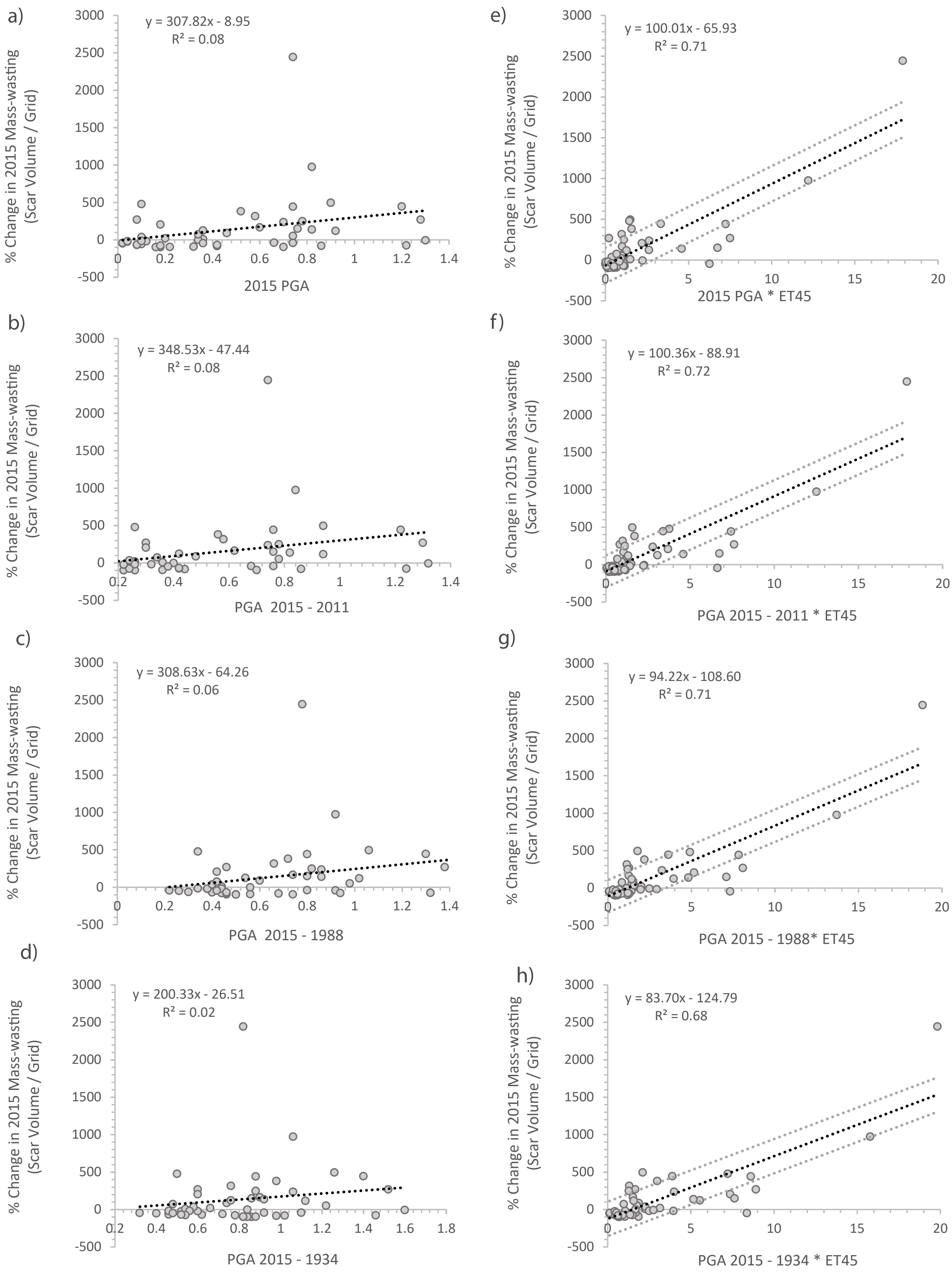
a)
y = 307.82x - 8.95
R² = 0.08
% Change in 2015 Mass-wasting (Scar Volume / Grid)
2015 PGA
b)
y = 348.53x - 47.44
R² = 0.08
PGA 2015 - 2011
c)
y = 308.63x - 64.26
R² = 0.06
PGA 2015 - 1988
d)
y = 200.33x - 26.51
R² = 0.02
PGA 2015 - 1934
e)
y = 100.01x - 65.93
R² = 0.71
2015 PGA * ET45
f)
y = 100.36x - 88.91
R² = 0.72
PGA 2015 - 2011 * ET45
g)
y = 94.22x - 108.60
R² = 0.71
PGA 2015 - 1988* ET45
h)
y = 83.70x - 124.79
R² = 0.68
PGA 2015 - 1934 * ET45

Figure 7 (above). Correlations between maximum summed PGA and excess monsoon-triggered 2015 mass-wasting for a) PGA in the 2015 main shock and largest aftershock. b) the summed PGA from a) plus the PGA from 2011. c) the summed PGA from b) plus the PGA from 1988. d) the summed PGA from c) plus the PGA from 1934. e – f) show the same correlations as a – d) but with summed PGAs multiplied by excess topography above a threshold angle of 45°. The linear best-fits are shown with +/- 1 standard error in each case.

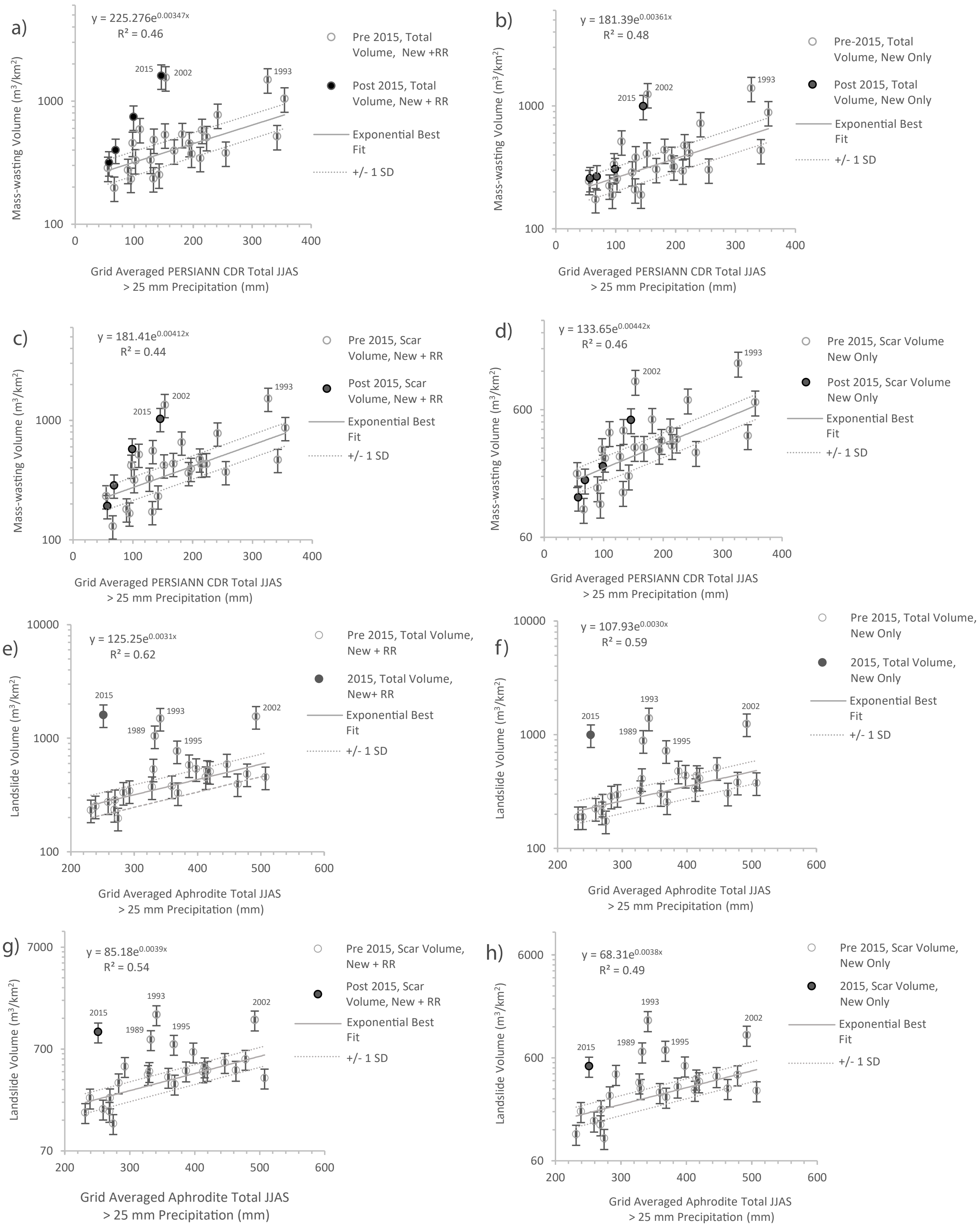

Figure S1. a – d) Empirical relationships between measures of mass-wasting volume (m^3/km^2) and PERSIANN-CDR total MJJAS precipitation > 25 mm for a) total "New + RR" volume, b) total "New Only" volume, c) scar "New + RR" volume and d) scar "New Only" volume. e – h) Empirical relationships between measures of mass-wasting volume (m^3/km^2) and APHRODITE total 15th June - Sept precipitation > 25 mm for e) total "New + RR" volume, f) total "New Only" volume, g) scar "New + RR" volume and h) scar "New Only" volume. Where, in all cases "New + RR" refers to the combined volumes of both new failures and reactivations/remobilisations and "New Only" refers to just the volumes of new failures, with reactivations and remobilisations excluded. The exponential best fits shown on these graphs apply to the non-anomalous pre-2015 points only, with all anomalous points labelled individually. The post-2015 points are also shown for reference, as are the +/- 1 standard errors on the fit equations.

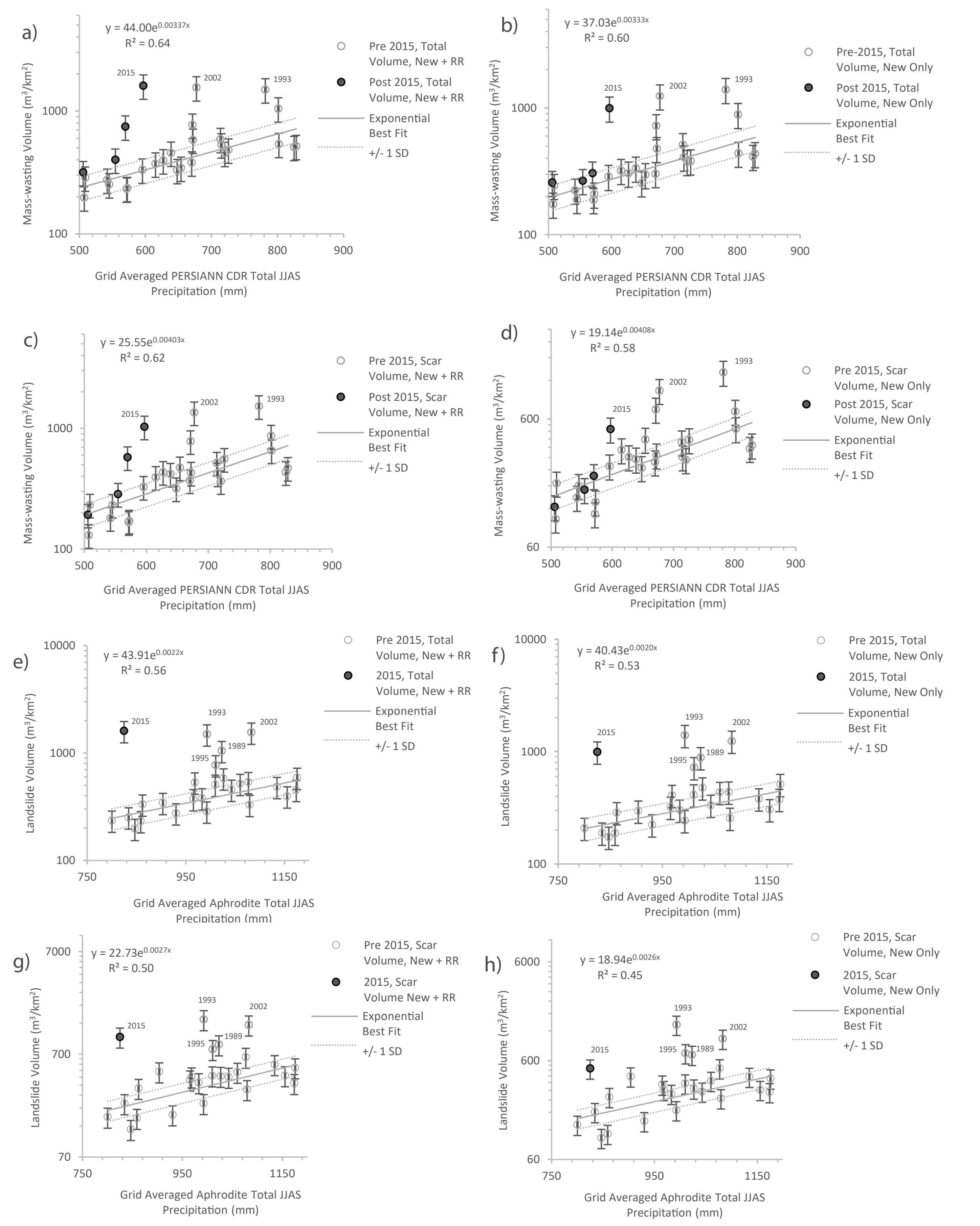

Figure S2. a – d) Empirical relationships between measures of mass-wasting volume (m³/km²) and PERSIANN-CDR total 15th June - September precipitation for a) total "New + RR" volume, b) total "New Only" volume, c) scar "New + RR" volume and d) scar "New Only" volume. e – h) Empirical relationships between measures of mass-wasting volume (m³/km²) and APHRODITE total 15th June – September precipitation for e) total "New + RR" volume, f) total "New Only" volume, g) scar "New + RR" volume and h) scar "New Only" volume. Where, in all cases "New + RR" refers to the combined volumes of both new failures and reactivations/remobilisations and "New Only" refers to just the volumes of new failures, with reactivations and remobilisations excluded. The exponential best fits shown on these graphs apply to the non-anomalous pre-2015 points only, with all anomalous points labelled individually. The post-2015 points are also shown for reference, as are the +/- 1 standard errors on the fit equations.

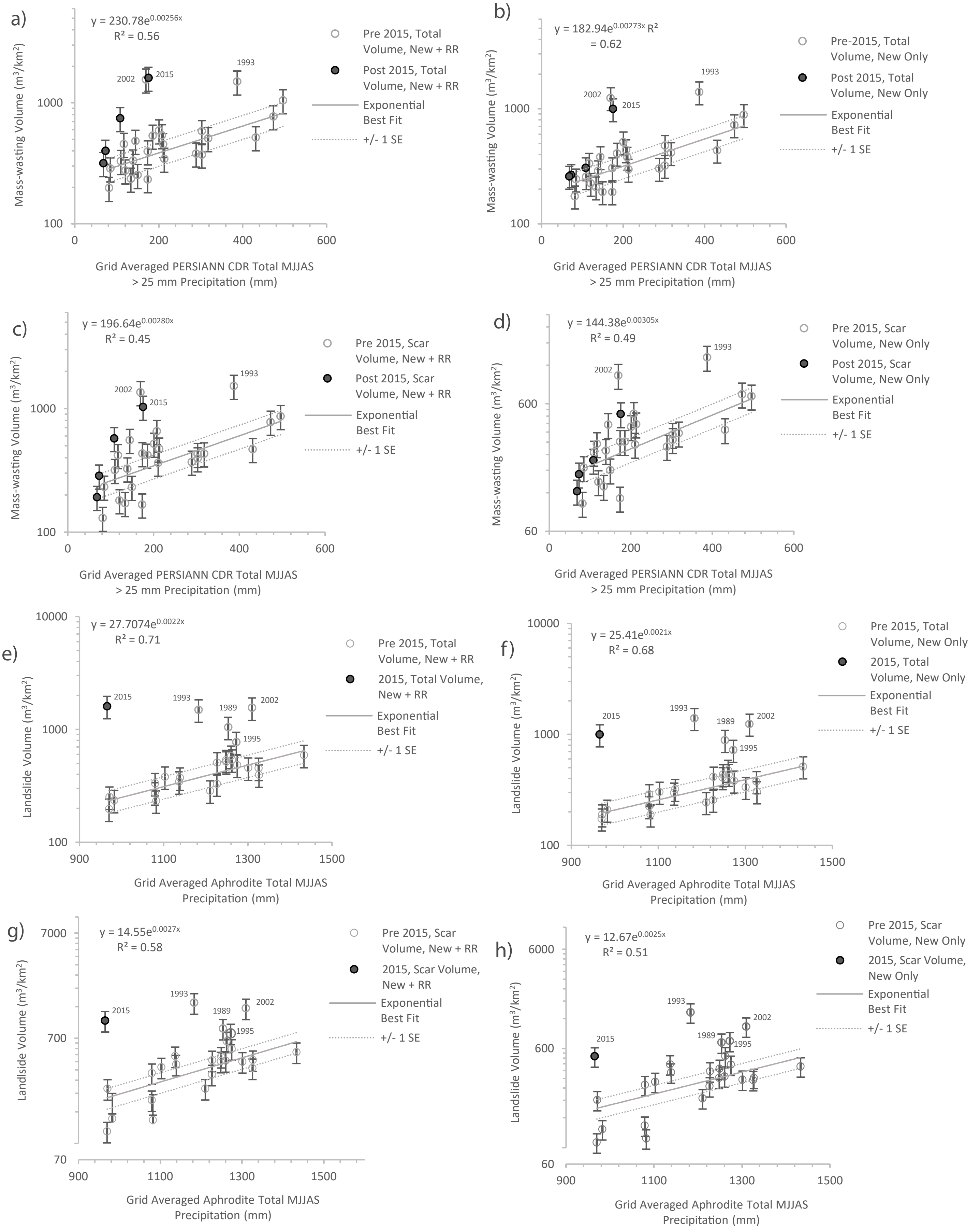

Figure S3. a – d) Empirical relationships between measures of mass-wasting volume (m³/km²) and PERSIANN-CDR total MJJAS > 25 mm precipitation for a) total "New + RR" volume, b) total "New Only" volume, c) scar "New + RR" volume and d) scar "New Only" volume. e – h) Empirical relationships between measures of mass-wasting volume (m³/km²) and APHRODITE total MJJAS precipitation for e) total "New + RR" volume, f) total "New Only" volume, g) scar "New + RR" volume and h) scar "New Only" volume. Where, in all cases "New + RR" refers to the combined volumes of both enw failures and reactivations/remobilisations and "New Only" refers to just the volumes of new failures, with reactivations and remobilisations excluded. The exponential best fits shown on these graphs apply to the non-anomalous pre-2015 points only, with all anomalous points labelled individually. The post-2015 points are also shown for reference, as are the +/- 1 standard errors on the fit equations.

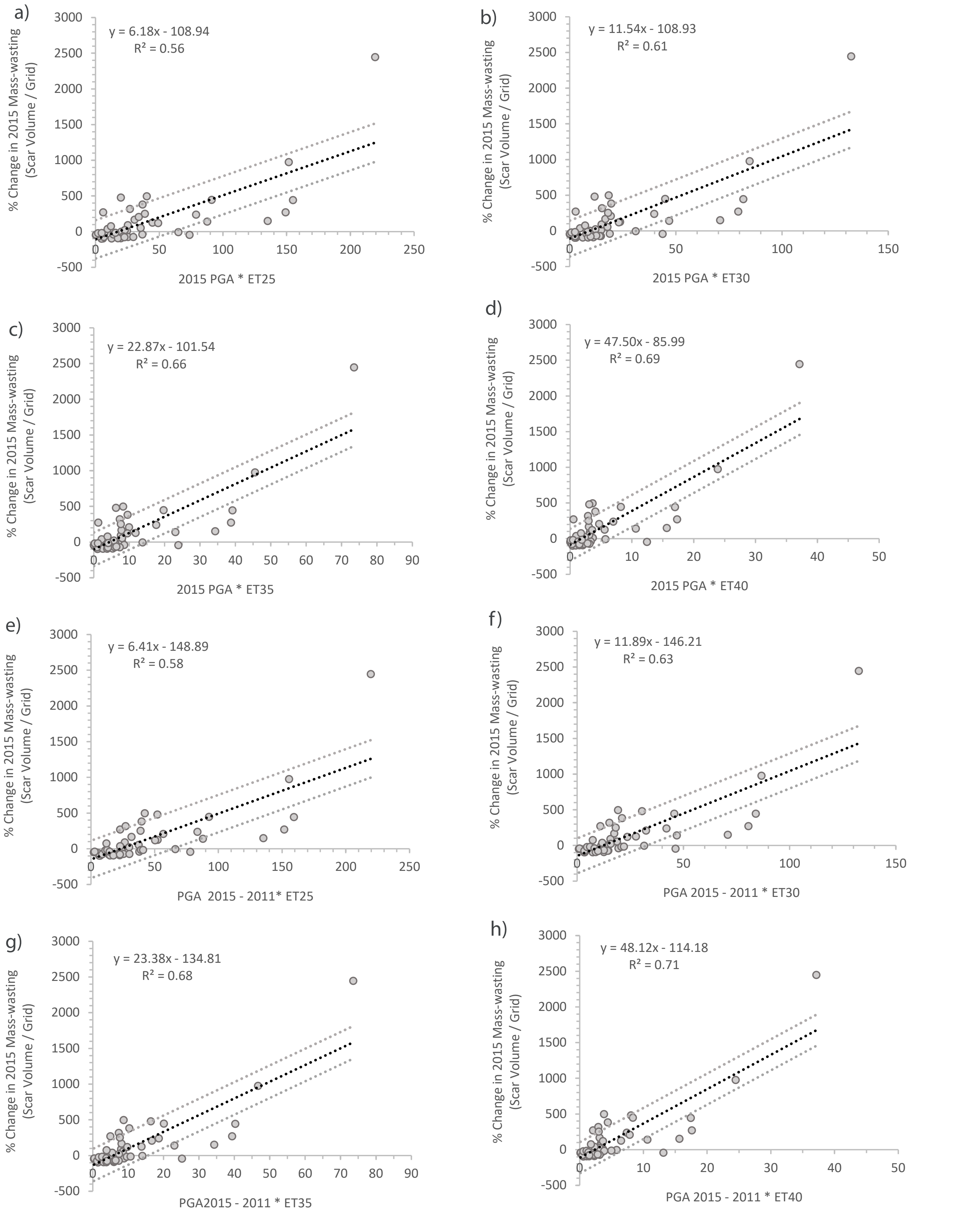

Figure S4. Correlations between excess monsoon-triggered mass-wasting in 2015 and maximum summed PGA in the 2015 main shock and largest aftershock multiplied by excess topography above a threshold angles of a) 25°, b) 30°, c) 35° and d) 40°. e – h) Correlations as in a – d) but with the PGA from the 2011 earthquake included in the summed PGA. The linear best-fits are shown with +/- 1 standard error in each case.

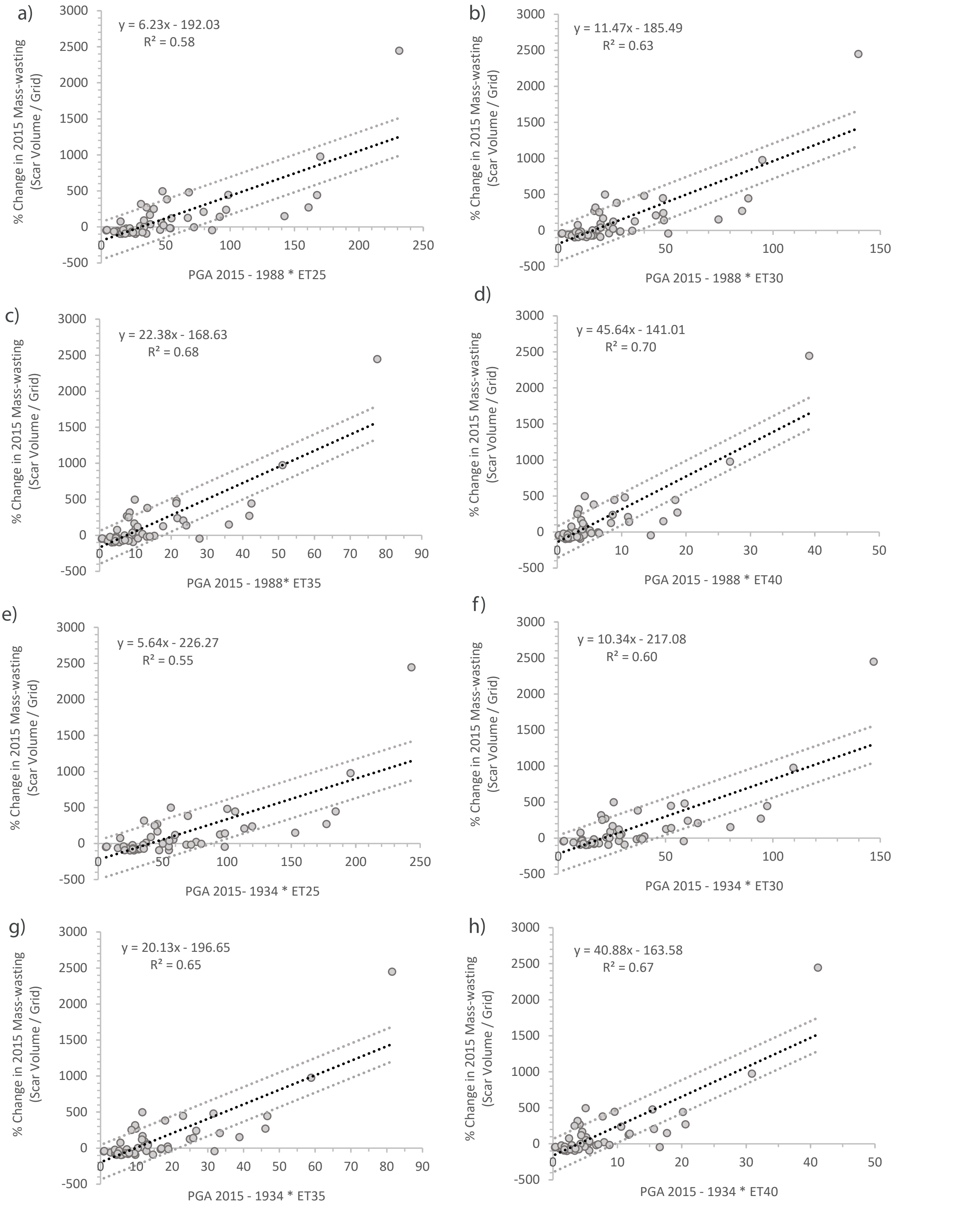

Figure S5. Correlations between excess monsoon-triggered mass-wasting in 2015 and maximum summed PGA in the 2015 main shock, 2015 largest aftershock, 2011 earthquake and 1988 earthquake multiplied by excess topography above a threshold angles of a) 25^{o}, b) 30^{o}, c) 35^{o} and d) 40^{o}. e – h) Correlations as in a – d) but with the PGA from the 1934 earthquake included in the summed PGA. The linear best-fits are shown with +/- 1 standard error in each case.

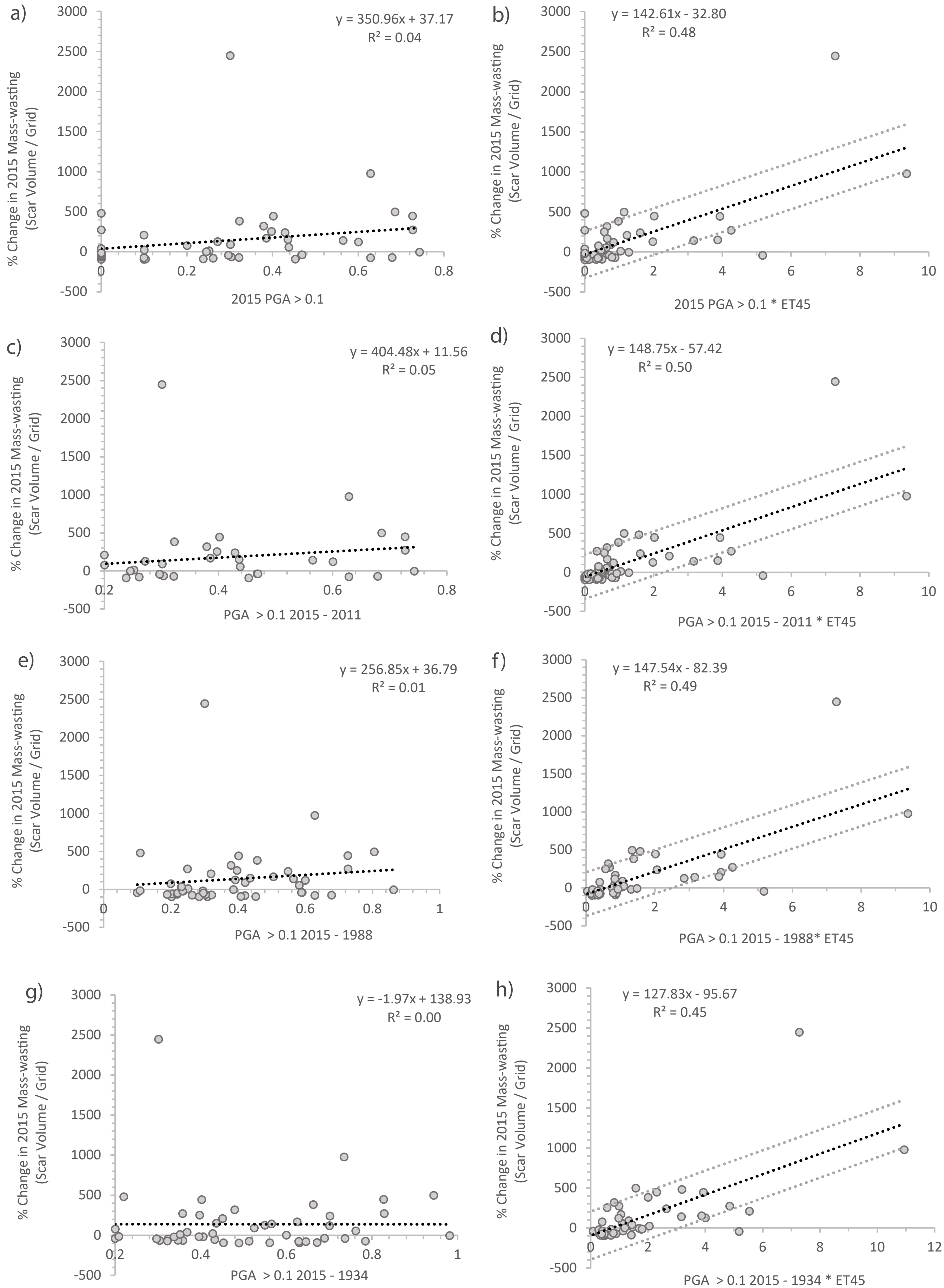

Figure S6. Correlations between excess monsoon-triggered mass-wasting in 2015 and summed PGA > 0.1 g in a) the 2015 main aftershock and largest aftershock, b) as a) but plus the 2011 PGA > 0.1 g, c) as b) but plus the 1988 PGA > 0.1 g, and d) as in c) but plus the 1934 PGA > 0.1 g. e – h) the same correlations in a – d) but with PGA multiplied by excess topography above a threshold angle of 45°.

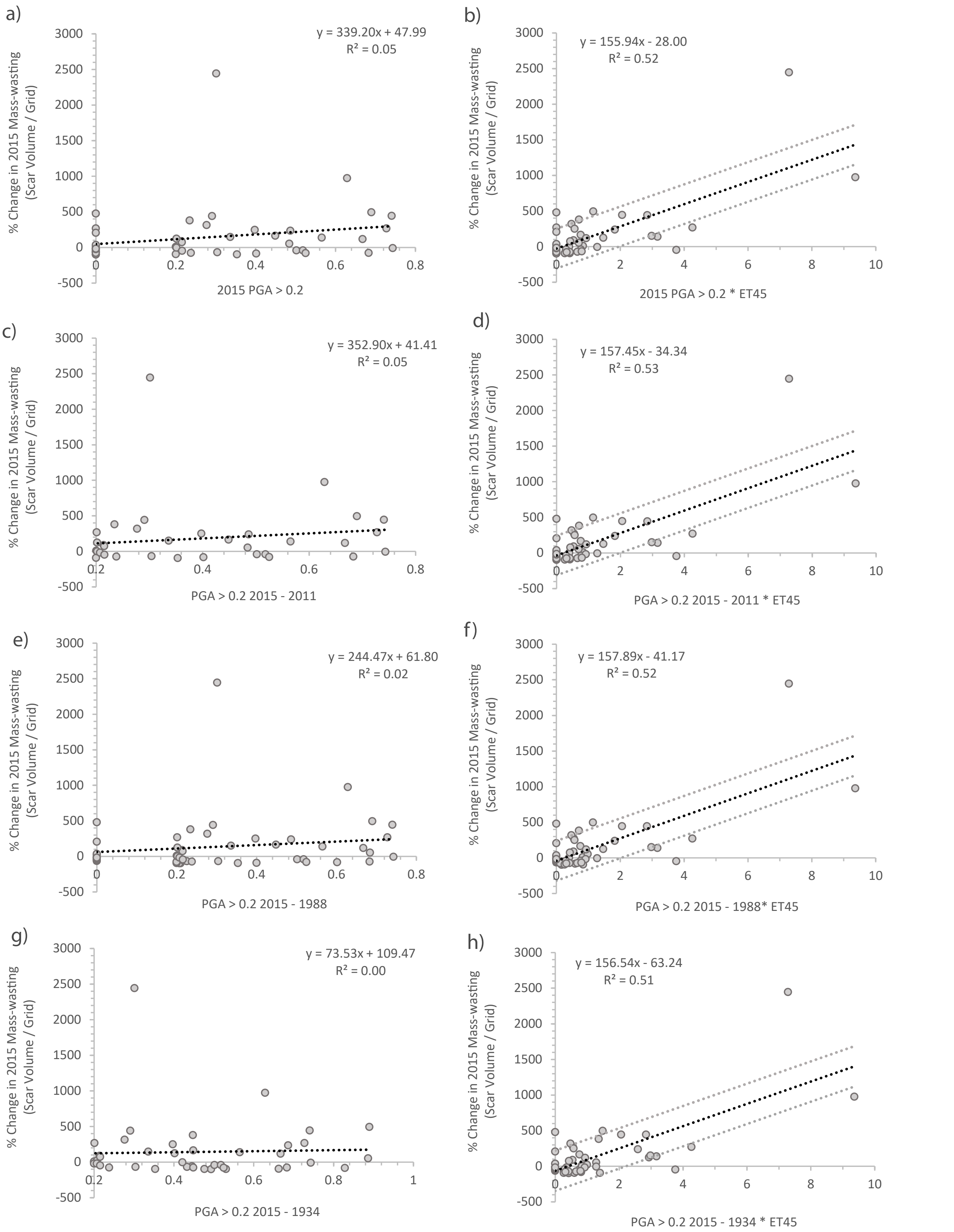

Figure S7. Correlations between excess monsoon-triggered mass-wasting in 2015 and summed PGA > 0.2 g in a) the 2015 main aftershock and largest aftershock, b) as in a) but plus the 2011 PGA > 0.2 g, c) as in b) but plus the 1988 PGA > 0.2 g, and d) as in c) but plus the 1934 PGA > 0.2 g. e – h) the same correlations in a – d) but with PGA multiplied by excess topography above a threshold angle of 45°.

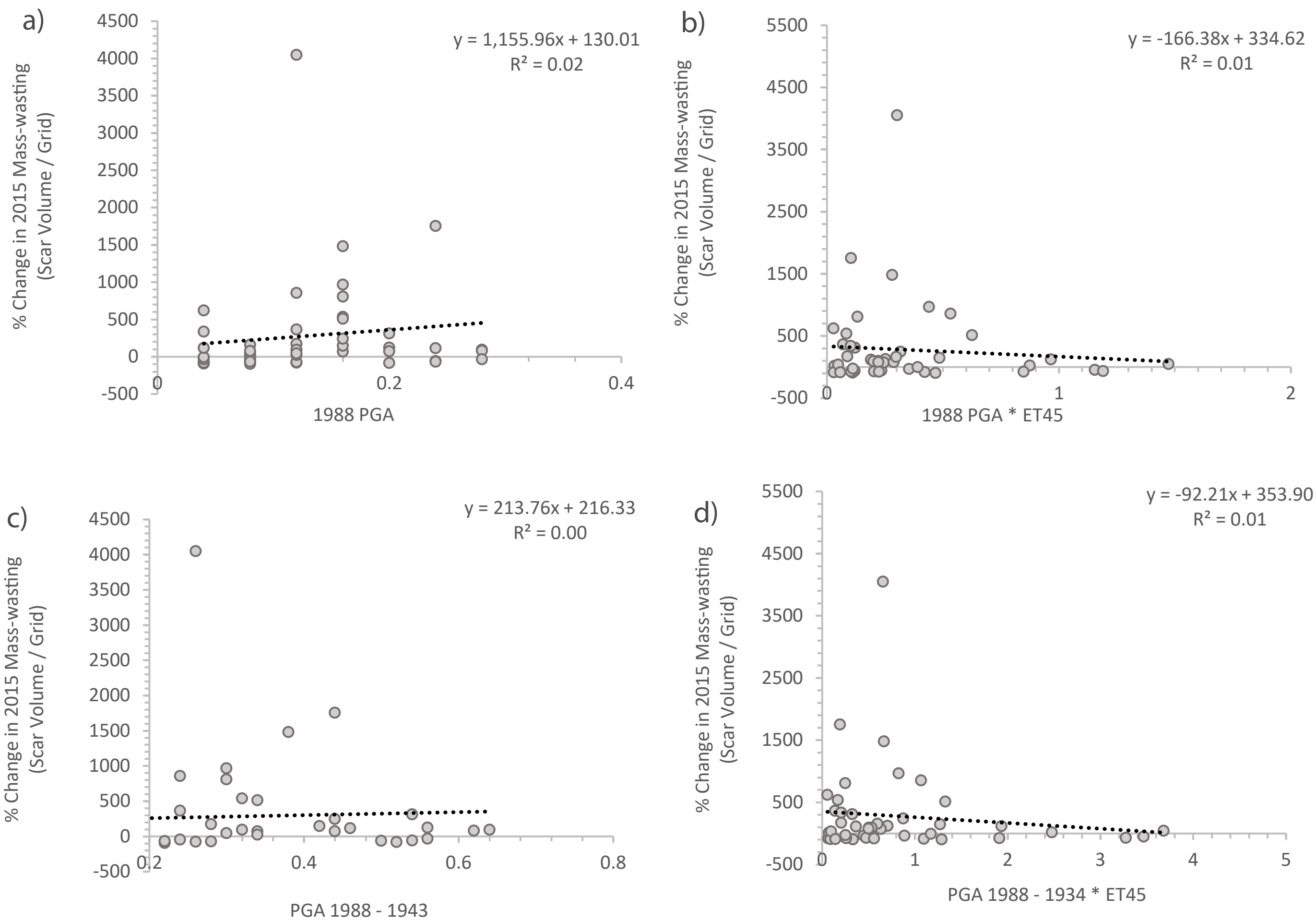

Figure S8. Correlations between excess monsoon-triggered mass-wasting in 1989 and summed PGA in a) the 1988 earthquake, b) the 1988 earthquake multiplied by excess topography above a threshold angle of 450, c) the 1988 ad 1934 earthquake, d) the 1988 and 1934 earthquakes multiplied by excess topography above a threshold angle of 45^{o}.

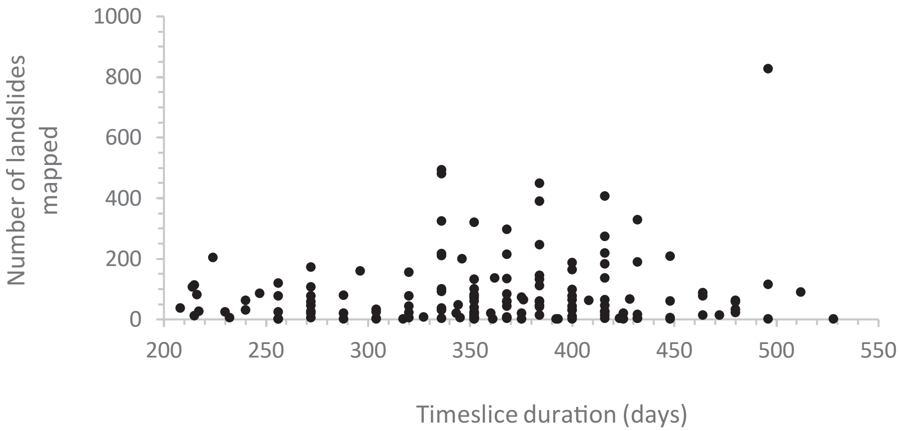

Figure S9 – Correlation between time slice length (where variation is due to varying numbers of days between October and April) and number of mapped features. We find no positive relationship between the two, suggesting that very few events occur between October and April, and thus that our varying time slice lengths do not unduly affect our analyses.

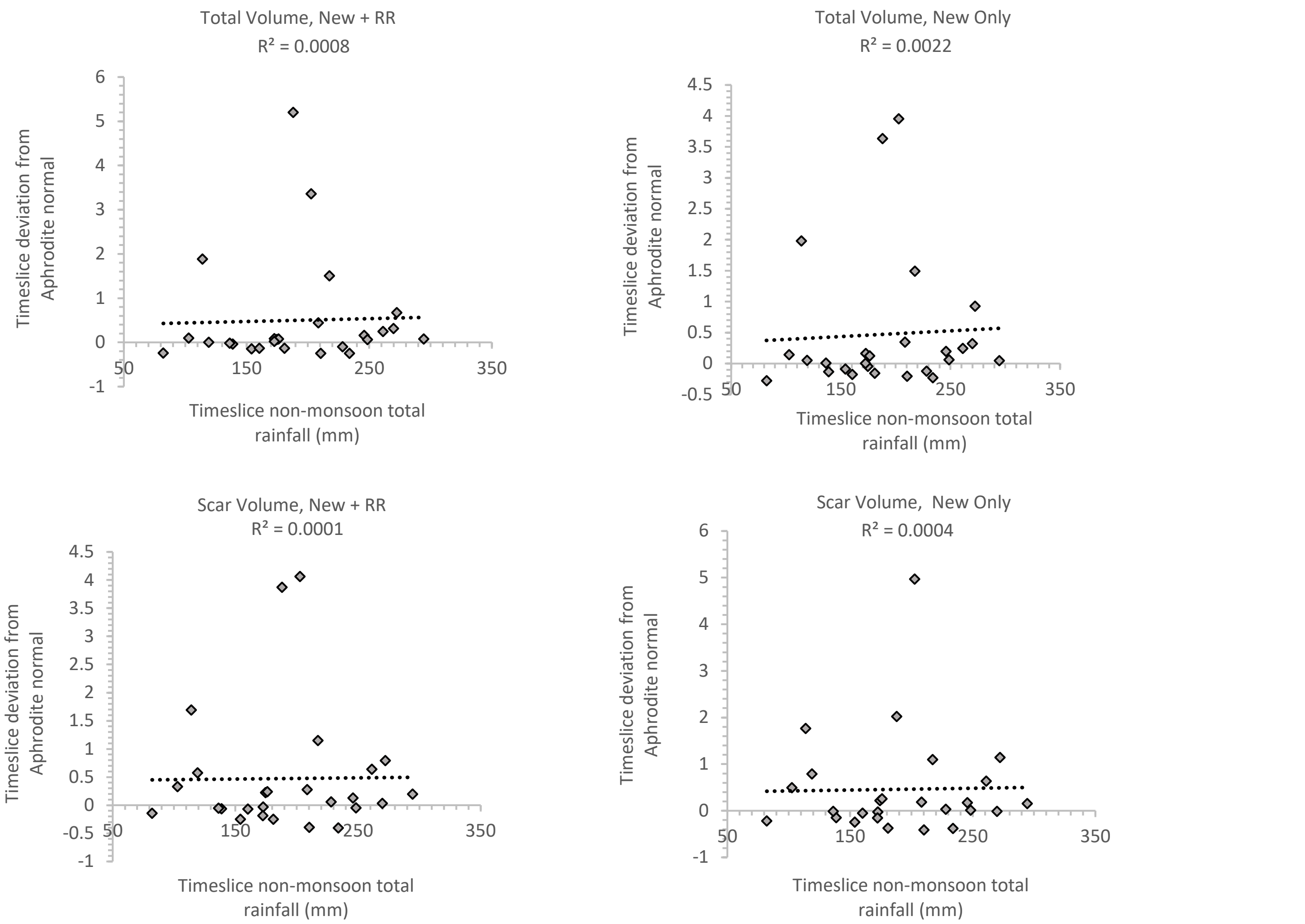

Figure S10 – Correlation between total rainfall in the non-monsoon months included in each mapping interval and the deviations from the normal in the normalised rate observed in figure 3b. We find no positive relationship between the two, suggesting that our varying time slice lengths do not unduly affect our analyses.

Year	No. Mapped Features	Total Volume "New + RR" (m^3)	Total Volume "New Only" (m^3)	Scar Volume "New + RR" (m^3)	Scar Volume "New Only" (m^3)	Satellite Product Used
1988	552	23842587	20327357	25329600	21316385	Landsat 4/5
1989	368	44606067	37795615	36977800	29307496	Landsat 4/5
1990	282	24798168	20356572	18248563	13367633	Landsat 4/5
1991	185	14664730	12655041	20171382	17717302	Landsat 4/5
1992	206	10757394	8060680	9882284	7721032	Landsat 4/5
1993	688	63706490	59524933	64963866	59052172	Landsat 4/5
1994	239	15881316	13668377	16828875	14655775	Landsat 4/5
1995	329	32881528	30801027	33287489	30403043	Landsat 4/5
1996	349	17878160	14024401	20811952	15219065	Landsat 4/5
1997	248	16196123	12896086	15801173	11798940	Landsat 4/5
1998	274	20637304	16252455	23724167	17550177	Landsat 4/5
1999	369	25149652	21853231	22080466	16885497	Landsat 4/5
2000	477	19763192	14557902	18940784	13471883	Landsat 7
2001	572	22742863	17444836	17995094	12919774	Landsat 7
2002	1337	66201168	52972260	57674509	42572127	Landsat 7
2003	297	19987080	16671775	17856598	14606480	Landsat 7
2004	564	22259342	18215714	20338658	16930196	Landsat 4/5
2005	149	9962131	8952169	7263236	5938146	Landsat 4/5
2006	206	14173187	12255139	13929565	10967058	Landsat 4/5
2007	211	22935697	18688172	27965378	21391510	Landsat 4/5
2008	216	12195684	10402270	9918266	8057466	Landsat 4/5
2009	175	11456406	9351355	9609328	6937638	Landsat 4/5
2010	310	14054953	10916087	13546765	10640480	Landsat 4/5
2013	433	9931421	8042592	7118385	4642711	Landsat 8
2014	507	20382998	18199991	25598549	24139158	Landsat 8
2015	1328	79809974	42454871	61102244	21285238	Landsat 8
2016	890	31772872	13029709	24516651	9213868	Landsat 8
2017	753	18691302	12983404	14089973	9062546	Landsat 8
2018	406	13507735	10991457	8200926	5270255	Landsat 8

Table S1 Summary of yearly mass-wasting data